MICROCOPY RESOLUTION TEST CHART

DOT/FAA/PM-87/11

AD-A185 839

A High Resolution Spatial and Temporal Multiple Doppler Analysis of a Microburst and its Application to Aircraft Flight Simulation

K. L. Elmore
J. McCarthy

Research Applications Program
National Center for Atmospheric Research
P.O. Box 3000
Boulder, CO 80307

and

Walter Frost
Ho-Pen Chang

FWG Associates, Inc.
Rt. 2, Box 271-A
Tullahoma, TN 37388

March 1987

This document is available to the public
through the National Technical Information
Service, Springfield, Virginia 22161

NOTICE

This document is disseminated under the sponsorship of the Department of Transportation in the interest of information exchange. The United States Government assumes no liability for its contents or use thereof.

1. Report No.	2. Government Accession No.	3. Recipient's Catalog No.
DOT/FAA/PM-87/11	AD-A185 839	

4. Title and Subtitle	5. Report Date
A High Resolution Spatial and Temporal Multiple Doppler Analysis of a Microburst and its Application to Aircraft Flight Simulation	March 1987
	6. Performing Organization Code

7. Author's)	8. Performing Organization Report No.
K. L. Elmore, J. McCarthy, W. Frost and H. P. Chang	

9. Performing Organization Name and Address	10. Work Unit No. (TRAIS)
Research Applications Program, NCAR P. O. Box 3000 Boulder, Colorado 80307	
	11. Contract or Grant No.
	DTFA01-82-Y-10513

12. Sponsoring Agency Name and Address	13. Type of Report and Period Covered
U.S. Department of Transportation Federal Aviation Administration Program Engineering and Maintenance Service Washington, D.C. 20591	Technical Report
	14. Sponsoring Agency Code
	APM-310

15. Supplementary Notes

16. Abstract

Multiple Doppler radar data collected during the Joint Airport Weather Studies (JAWS) Project are used to synthesize the three-dimensional wind in the region of a microburst. The particular microburst used in this study is the strongest one to date for which three-dimensional winds have been recovered. As a diagnostic tool, a six-degree-of-freedom numerical aircraft model having characteristics similar to Boeing 727 series aircraft is used to investigate jet transport aircraft response to observed microburst winds during simulated approaches and departures. Simple pilot control laws are used to adjust thrust, pitch, roll, and yaw so as to maintain given approach or departure parameters. Generally, when horizontal wind shear along the approach or departure path is 10×10^{-3} s^{-1} or greater, the model is unable to maintain the desired approach path and suffers a significant reduction in climb performance during a go-around or departure. Although the mean wind shear along a path gives a good qualitative measure of the wind shear threat to a jet transport, different paths with similar mean shears can yield markedly different results, as do the same paths through the microburst at different times. These findings are a direct consequence of the fine temporal and spatial scale of microburst winds. During any given modelled aircraft traverse through the region of highest horizontal shear, time variations in the microburst wind field are shown to have an insignificant effect on the modelled flight path. This is because the traverse period is short (30 s) compared to the lifetime of a microburst (300-600 s).

17. Key Words	18. Distribution Statement
Microburst, Doppler radar, simulation, wind shear, divergence, aircraft, approach, departure, airspeed, model	This document is available to the public through the National Technical Information Service, Springfield, Virginia 22161.

19. Security Classif. (of this report)	20. Security Classif. (of this page)	21. No. of Pages	22. Price
Unclassified	Unclassified	59	

Form DOT F 1700.7 (8-72)   Reproduction of completed page authorized

Table of Contents

List of Tables

List of Figures

1. Introduction

a. Accidents and Incidents Attributable to Microburst Wind Shear

From 1964 to 1982 twenty-four wind-shear related accidents and three incidents occurring in airport terminal areas involving large – gross weight greater than 5670 kg – transport aircraft have been identified from 19,332 National Transportation Safety Board reports of accidents and incidents. These 24 accidents resulted in 491 fatalities and 206 injuries, accounting for nearly all the fatalities suffered by the air carrier industry (National Research Council, 1983).

Microbursts* were first recognized as an aircraft hazard by an Australian Bureau of Air Safety investigation of an accident that occurred at Bathurst, New South Wales, on 31 May 1974. A Fokker F-27 crashed as it attempted a go-around after experiencing difficulty during its approach (Department of Transport, Australia, 1977). From the pilot's description, eyewitness accounts, and the very limited information from the Flight Data Recorder (FDR) on board the aircraft, the Bureau determined that the crash was caused by strong, diverging horizontal winds that resulted when a downdraft penetrated to the surface. Similar small-scale outflows had been identified twenty-five years previously during the Thunderstorm Project (Byers and Braham, 1949). However, the low-altitude wind shear hazard was not fully appreciated until the crash of Eastern Airlines (EAL) Flight 66 on approach to John F. Kennedy International Airport on 24 June 1975 (Fujita and Byers, 1977; Fujita, 1983a).

Analysis of FDR records from EAL Flight 66 and aircraft in the immediate vicinity provided a wind model believed similar to that encountered by EAL Flight 66 (NTSB, 1976). This model consisted of an intense, small-scale downdraft descending to very near the ground and spreading out horizontally. Fujita (1976) coined the term downburst to describe this phenomenon.

Figure 1 shows a schematic representation of typical jet transport aircraft response when encountering a microburst during departure. As the airplane accelerates down the runway, it experiences an increasing headwind. It lifts off in this increasing headwind and begins to climb (position 1). Near position 2, it begins to encounter the microburst downdraft resulting in decreased climb performance. By position 3, the headwind has been lost, decreasing airspeed and reducing lift and climb performance further. Added to this is the increased downdraft at the microburst center. Due to the continued tailwind increase, all available energy is needed to maintain flight by position 4; none is available to add potential energy (climb) to the airplane. An airplane is typically configured ("trimmed") such that thrust, drag, lift, and weight are all in equilibrium. Thus, no pilot input is required for the airplane to maintain a set trajectory. Since airspeed is below the trim airspeed at position 4 (decreasing lift and drag), the airplane system will respond so as to

---

* In this study the definition of a microburst is modified to refer to Doppler radar-observed diverging outflows near the surface associated with convective storms. The peak-to-peak differential Doppler velocity across the divergence center must be >10 m s^{-1} and the initial distance between maximum approaching and receding centers must be <4 km. These criteria differ slightly from Fujita's original definition.
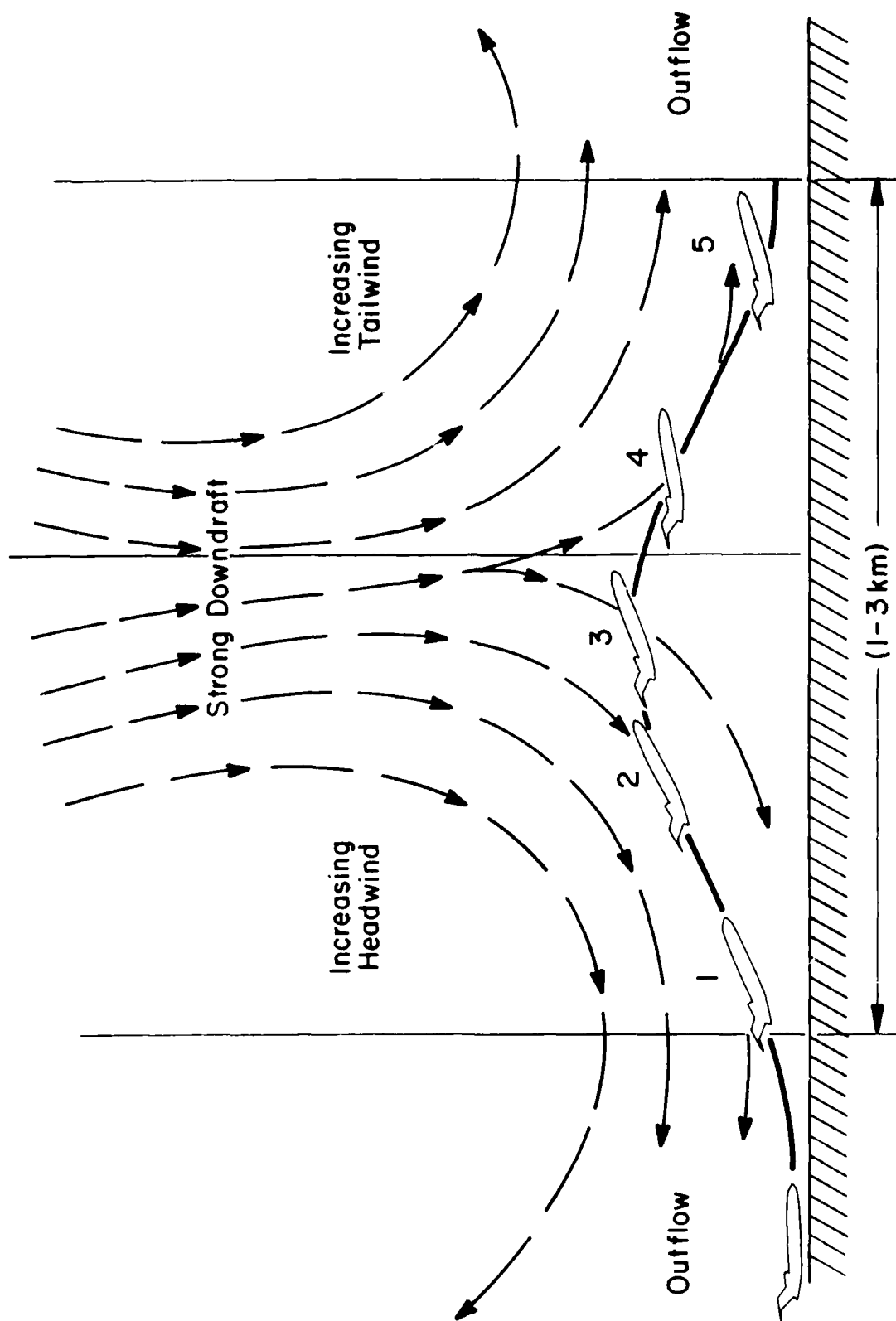
FIGURE 1. Typical jet transport aircraft response to microburst wind shear during departure. After lifting off in an increasing headwind at 1, it begins to lose the headwind and enter the downdraft at 2, experiences stronger headwind loss at 3 with subsequent arrest of climb, begins descending in increasing tailwind at 4, and experiences an accelerating descent rate through 5.

2

regain the equilibrium condition by pitching the nose downward. If the pilot does not fully compensate for this (as shown), a descent rate above that which would occur with proper compensation can result. This descent rate continues to increase as the airplane passes through position 5. Depending on the strength of the event, encounter altitude, aircraft performance margin, and most importantly, how quickly the pilot recognizes and reacts to the hazard, the resulting high descent rate may be impossible to arrest before ground impact. Thus, during an approach a typical response upon encountering a microburst, with no *a priori* knowledge of the hazard and in the absence of wind shear training, may aggravate an already hazardous situation.

Pan American World Airways (PAA) Flight 759 is a recent example of a fatal microburst-induced departure accident; its flight trajectory is the basis for Fig. 1. PAA Flight 759 crashed while departing from Moisant Field near New Orleans, Louisiana, on 9 July 1982 killing 159 and injuring 9. Analyses by Fujita (1983a), Caracena *et al.* (1983) and the National Transportation Safety Board (NTSB, 1983) showed the cause of the PAA Flight 759 crash to be a convective microburst of average intensity over a shorter-than-average distance: a 23 m s^{-1} vector velocity difference over a 1.5 km distance.

During the Joint Airport Weather Studies (JAWS) Project, an average microburst had a shear of 24 m s^{-1} over a 3.1 km distance (Wilson *et al.*, 1984). The microbursts encountered by EAL Flight 66 and PAA Flight 759 occurred during thunderstorms, but many microbursts originate in benign-appearing clouds. On 7 August 1975 an accident occurred involving Continental Airlines (CO) Flight 426 as it departed Stapleton International Airport in Denver, Colorado. This flight encountered a serious wind shear immediately after liftoff, resulting in a crash off the end of the departure runway (there were no fatalities and only fifteen injuries). A shower over the airport produced only a small area of light rain on the runway (Fujita and Caracena, 1977). The JAWS Project observed similar microburst occurrences during its field project in the summer of 1982 (Wilson *et al.*, 1984).

b. The JAWS Project

The JAWS Project addressed the microburst problem from both scientific and applied aviation hazard perspectives (McCarthy *et al.*, 1982). Focusing specifically on microbursts, the field program was conducted near Stapleton International Airport between 15 May and 13 August 1982. The primary instruments were three NCAR pulsed Doppler radars: CP-2 (10 cm), CP-3, and CP-4 (both 5 cm). All three radars have 1° nominal beam widths.

Figure 2 shows the configuration of the radar network used in JAWS and the location of the data grid containing the microburst discussed below. Doppler data used here are from CP-3 and CP-4 only. The baseline distance between CP-3 and CP-4 is 14.7 km; CP-3 is 14.15 km east and 11.19 km south of CP-2 while CP-4 is 10.43 km east and 25.45 km south of CP-2. CP-4 was deployed near the center of Stapleton International Airport.

3
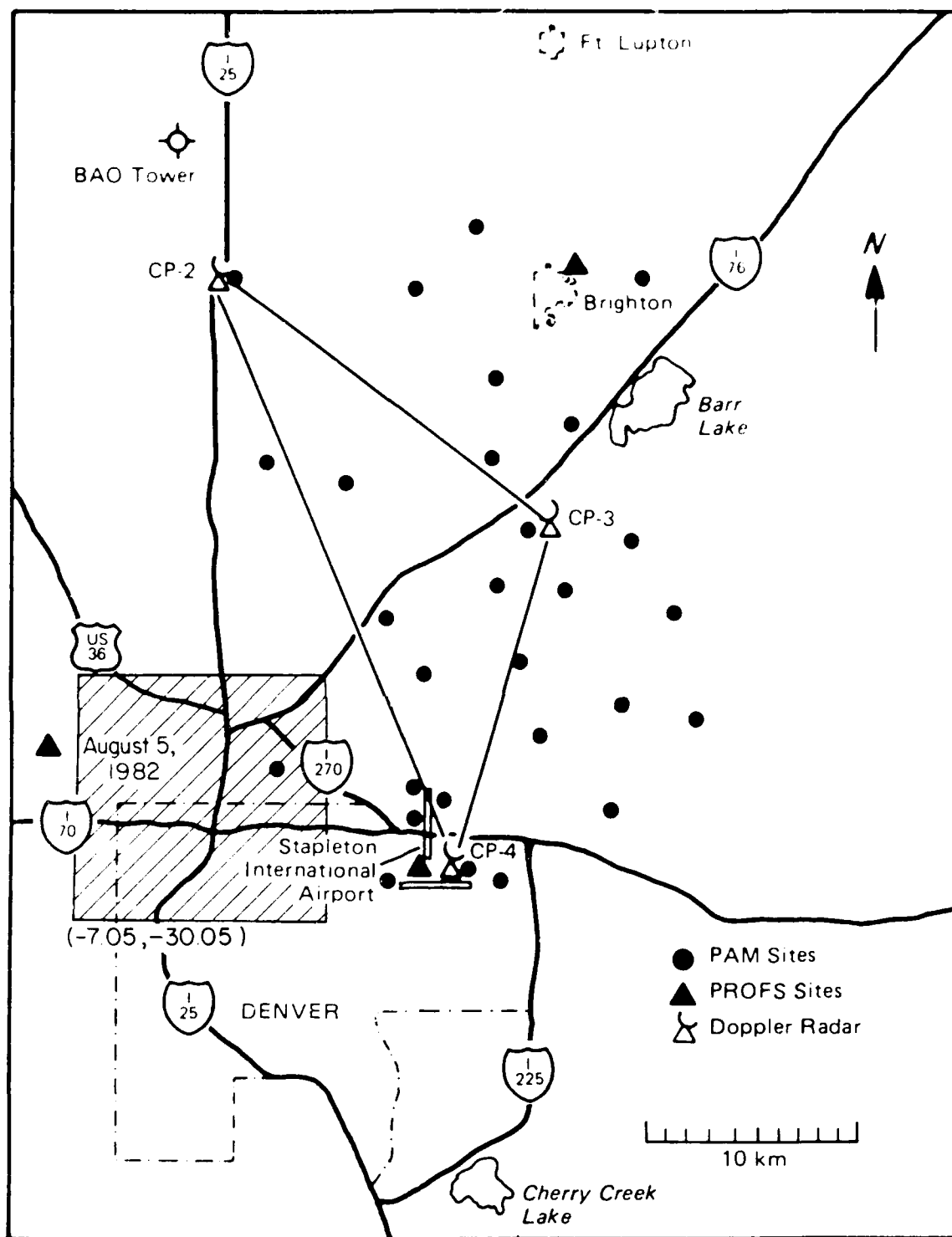
FIGURE 2. JAWS network showing radar positions relative to the analysis region. Only data from CP-3 and CP-4 are used. Cross-hatched region shows area over which dual-Doppler synthesis was performed. Numbers in parentheses are (x, y) coordinates of lower left-hand corner relative to CP-2.

c. Current Wind Shear Data Limitations

Pilot training, when addressing hazardous wind shear, has stressed avoidance. Thunderstorms receive particular attention since they are known to contain destructive turbulence and hail along with unpredictable surface winds. However, because microbursts can and do occur in innocuous-appearing weather conditions, visual avoidance will not always be possible. Until there are *in situ* and/or remote sensors that properly detect and locate the hazard, these necessary avoidance procedures will be nearly impossible to implement.

Flight simulators provide a unique pilot training opportunity in that they can utilize the high spatial and temporal resolution data available from multiple Doppler analyses. Modern flight simulators are driven by small computers, which solve relatively sophisticated numerical models describing the flight of particular types of jet transport aircraft. These models include the effects of a pilot's control inputs and external effects such as wind shear. Thus, actual multiple-Doppler analyzed winds can be input to the flight simulator computer, creating the external effects caused by microburst-type wind shear.

Prior to the JAWS Project, essentially all convective storm, low-altitude wind shear data used for pilot training and computer-modelled flight profiles came from two sources: FDR derived profiles and profiles from tall instrumented towers.

FDR profiles are obtained by making a number of assumptions, often using best-guess values which may not accurately reflect conditions. Most recorders currently in use record only time, vertical acceleration, magnetic heading, altitude, and indicated airspeed (IAS). Expected aircraft performance in a stable (no shear) wind field is dependent on aircraft configuration. *i.e.*, flap setting, landing gear up or down, weight, and thrust. Values for these parameters are usually assumed. Because of these assumptions and lack of inertial longitudinal acceleration data the resultant three-dimensional wind solution is not unique. Consequently, implausibly large downdraft velocities exist near the ground in some low-altitude wind shear profiles currently used in flight simulation, as an artifact of these assumptions. Finally, because the resulting wind field is essentially one-dimensional, multi-dimensional characteristics must be subjectively described in any FDR wind model.

Wind profiles also come from the instrumented tower near Oklahoma City, Oklahoma, operated by NOAA's National Severe Storms Laboratory (Frost and Camp, 1977; McCarthy *et al.*, 1979). Most of these data were collected at seven levels – from the surface to approximately 450 m - during thunderstorm situations and most of these profiles have involved gust front phenomena. Since the tower is geographically fixed, the passage of any weather event is measured in the two-dimensional plane of the tower location (Goff, 1975) and time stationarity is assumed to obtain the two-dimensional flow field. Another limitation results from the inherent averaging of data collected at the tower, typically one minute for most of the derived models. For an event translating at 10 m s^{-1}, this yields a 600 m spatial sampling interval. To date none of these tower-derived wind field models contain a microburst.

SRI International used convective storm data from the above two sources to arrive at the best current wind shear models for use in pilot recurrent training and testing of airborne wind shear detection and warning devices (Foy, 1979). Because of the previously

5

outlined data-base limitations, a major JAWS Project objective was to collect and make available higher resolution, more realistic wind shear fields.

In Section 2, a single microburst event is analyzed at four different times, each 2 min apart, with the highest horizontal and vertical resolution possible. Pertinent meteorological characteristics, such as downdraft strength, horizontal outflow scale, horizontal outflow wind speeds, equivalent radar reflectivity factor (dBZ_e) and their change with time will be quantified and discussed. In Section 3, these high resolution multiple Doppler data are applied to the problem of flight simulation using a realistic numerical aircraft model. Results of these simulations are discussed in light of the meteorological characteristics of this microburst.

2. 5 August 1982 Data Analysis Results

a. General Characteristics

Microburst data were collected by CP-3 and CP-4 on 5 August 1982. The maximum radial velocity differential, $\frac{\Delta V_r}{\Delta r}$ (also the maximum headwind-to-tailwind change), is 32 m s^{-1} over 2.3 km (average shear of 14×10^{-3} s^{-1}), stronger than the mean intensity observed by Wilson et al. (1984) of 24 m s^{-1} over 3.1 km (7.7×10^{-3} s^{-1} average shear). This is an acceptable case for flight simulation work since Frost and Bowles (1984) and Frost (1983) have shown that jet transport aircraft are strongly affected by shears on the order of 10×10^{-3} s^{-1}. Additionally, this case is relatively free of other low-altitude wind shear events, and occurs in almost quiescent mean surface flow. The viewing angle between CP-3 and CP-4 is from 40° to 60° in the immediate microburst vicinity, yielding acceptable error variances generally less than 1.0 m^2 s^{-2} (Doviak et al., 1978).

At 0.0° antenna elevation angles, near the microburst center, the CP-4 radar beam is 207 m in diameter centered 60 m above the surface and the CP-3 beam is 350 m in diameter with a center 55 m above the surface. These estimates are based on 1° beam widths and topography data taken from United States Geological Survey quadrangle maps using a lowest effective elevation angle of 0.2°; due to absorbtion of energy at 0.0° antenna elevation angles by the ground targets in the lower half of the beam, the lowest *effective* elevation angle of 0.2° is used (Wilson et al., 1984). Thus, the lowest grid level winds represent winds between 30 and 100 m above the surface. These winds are placed at the 0.0 km grid level because simulators must have continuous data extending upward from the surface.

Analysis of the 5 August microburst was done using a dual-Doppler analysis package described in Wilson et al. (1984). The scanning strategy for the two radars consisted of coordinated constant elevation sector scans that began and ended at nearly identical times, starting at an elevation angle 0.0°. Each elevation step was approximately 0.8 . Four individual analyses were done, each approximately 2 min apart. In no case did one radar begin or end its scan more than 15 s ahead of or behind the other. Analysis times are defined as 1845, 1847, 1850, and 1852 Mountain Daylight Time (MDT) covering the

Analysis Time (MDT)	Maximum Reflectivity at 0 m (dBZ$_e$)	Maximum Downdraft at 250 m (m s^{-1})	Maximum $\Delta V_r/\Delta r$ at 0 m
1845	54	-10	30 m s^{-1}/1.8 km
1847	58	-13	32 m s^{-1}/2.3 km
1850	57	-9	33 m s^{-1}/3.0 km
1852	56	-6	25 m s^{-1}/2.6 km

Table 1. Gross Microburst Characteristics.

event lifetime. Gross characteristics of the microburst at these times are shown in Table 1.

Resolution considerations dictated 150 m horizontal and 250 m vertical grid intervals. Scanning extended only slightly above 2.0 km, near the expected cloudbase as computed from the morning thermodynamic sounding. CP-2 is the origin ($x = 0$ km, $y = 0$ km) for all analyses. Figure 2 shows the data grid location with respect to the JAWS radars. Positive x is east and positive y is north. All locations are relative to CP-2 unless noted otherwise. The microburst center did not move significantly during the six minute period covered by these analyses.

b. 1845 Analysis Time

Figure 3a shows horizontal velocity vectors overlaid by reflectivity on the 0.0 km grid level (north is towards the top of the figure). Recall that the 0.0 km grid level winds are necessarily computed from observations between 30 and 100 m above the surface. A small bias error in w will result due to under-estimation of horizontal divergence. Vertical velocity will have a small positive bias in downdraft areas ($w < 0$) while in updraft areas ($w > 0$) w will have a small negative bias. For example, failure to sample a mean divergence of 10×10^{-3} s^{-1} over a 50 m depth will result in a positive bias in a downdraft of slightly more than 0.5 m s^{-1} at 500 m. Note also that the analysis area shown is a subvolume taken near the center of the entire analysis area shown in Fig. 2.

A reference velocity vector is shown in the upper right-hand corner and reflectivity is contoured in 10 dBZ$_e$ intervals. Note that the microburst is an extraordinarily small-scale phenomenon.

At the lowest analysis level, maximum divergence ($> 40 \times 10^{-3}$ s^{-1}) associated with this microburst is near $x = -1.5$ km and $y = -23.9$ km, defined as the microburst center. The microburst is asymmetric, with strong surface flow towards the southeast and northwest. Some weaker flow is seen towards the northeast. Reflectivity factor near the microburst center is in excess of 53 dBZ$_e$, indicating heavy rain and possibly some hail.

An aircraft flying through this microburst would experience much more serious wind shear along a northwest-southeast oriented track than along a northeast-southwest oriented track. Maximum 0.0 km vector velocity change across the microburst at this time (bold,
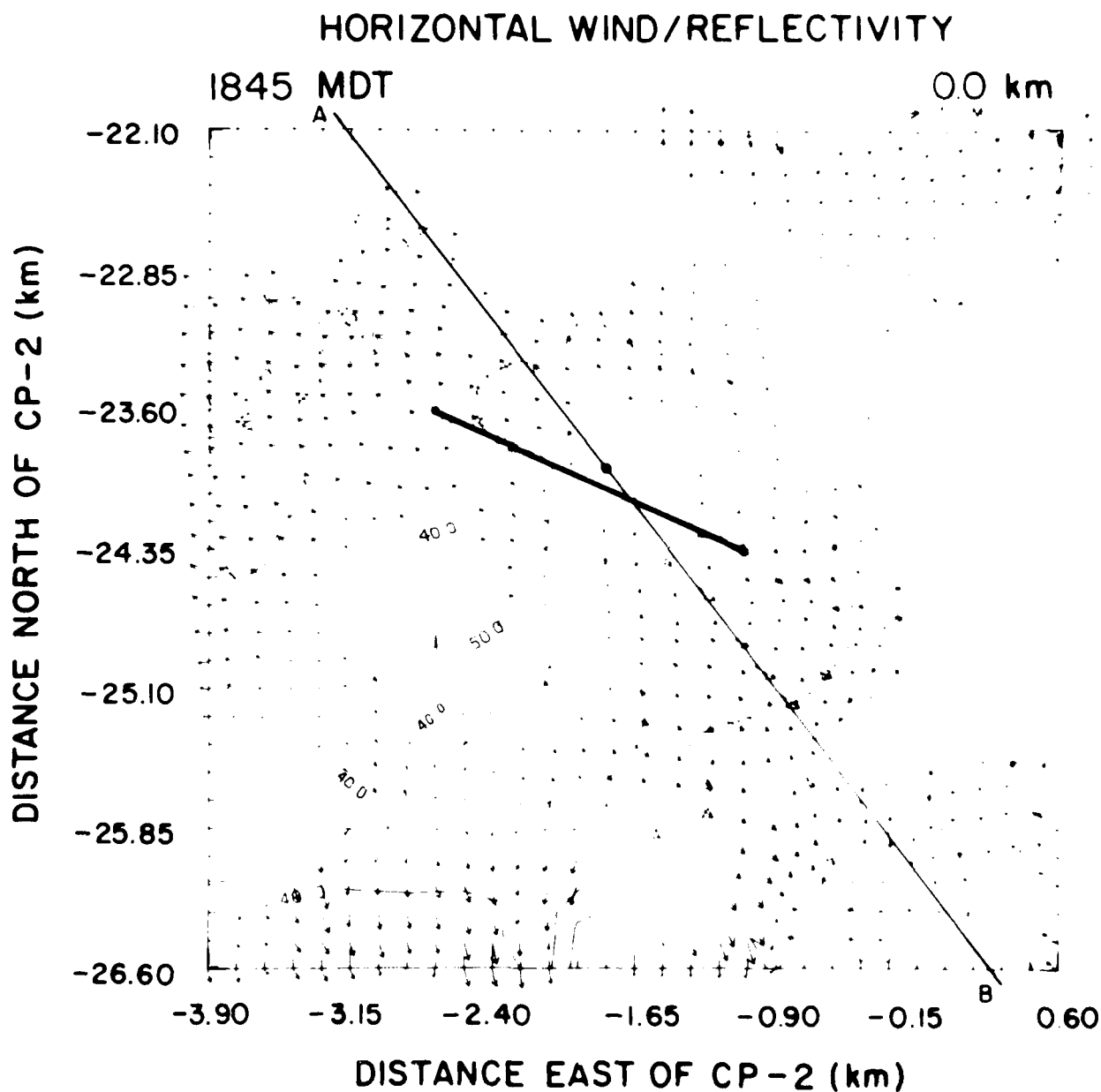
7

FIGURE 3A. 1845 MDT analyzed horizontal wind at 0.0 km height overlaid by reflectivity contoured in 10 dB intervals. Maximum $\frac{\Delta V_i}{\Delta r}$ shown by short heavy line. Line labeled AB is flight path that was tested; heavy dot shows location of path reference point at (x_{ref}, y_{ref}). Reference vector is in upper right corner.

8

dark line in Figure 3a and all subsequent horizontal cross sections) is 30 m s^{-1} over a distance of 1.8 km yielding an average shear of 17×10^{-3} s^{-1}. The other path, marked AB, is discussed later. Single Doppler radar observations along this line would show the maximum peak-to-peak approaching and receding flow (max $\frac{\Delta V_r}{\Delta r}$). Outflow shape and asymmetry is not easily explained; the microburst downdraft reached the surface in a residential region of Denver and local topography does not dictate these flow characteristics.

Figure 3b shows vertical velocity, wind vectors and reflectivity at the 250 m level. Hatching shows downdrafts greater than 5 m s^{-1}, while cross-hatching, which does not appear in Fig. 3b, indicates downdrafts stronger than 10 m s^{-1}. Stippling indicates areas of updraft greater than 5 m s^{-1}. As before, a bold, dark line marks the maximum average shear path at the 250 m level while the line marked AB shows a flight path that was tested, similar to Fig. 3a. Maximum downdraft velocity associated with the microburst is 10 m s^{-1}. Although this analysis cannot resolve the actual downdraft profile between 0.0 and 0.25 km, the downdraft will not be much stronger than 10 m s^{-1} anywhere between 0.0 km and 0.25 km and will decrease to zero at the surface. The shape of the downdraft does not afford a complete explanation of the asymmetry, as the area of $w < -5$ m s^{-1} is roughly ellipsoidal, with the major axis oriented SW–NE, about 1.5 km long, and the minor axis about 1 km long.

Maximum vector velocity change across the microburst along the path shown is 25 m s^{-1} over 2.1 km, 12×10^{-3} s^{-1} average shear. An aircraft will experience an increasing wind shear problem as it descends through this microburst. Maximum reflectivity values associated with the microburst at this level are nearly 55 dBZ$_e$.

Figure 3c shows a vertical cross section of this microburst in schematic form, similar to Wilson et al. (1984). These cross sections are shown for each analysis time, taken along a northwest-southeast oriented track. Schematic cross sections are made up of 3 or 4 individual cross sections since any single vertical cross section may not show all relevant features of this microburst. Individual cross sections are shown later. The cross section is viewed from the southwest so that the northwest side of the microburst is to the left and the southeast side is to the right. Each cross section extends vertically from the surface to 1 km and spans a horizontal distance of 10.5 km. The vertical dimension has been stretched by a factor of eight compared to the horizontal. Stippling indicates wind speeds 7.5 m s^{-1} or greater, and hatched areas show wind speeds of 12.5 m s^{-1} or greater. Large curls are observed on the outflow boundaries, similar to those in Wilson et al. (1984) and Fujita (1983b). These curls are ubiquitous, and have horizontal and vertical scales of about 1 km.

Any downdraft stronger than 12.5 m s^{-1} is limited to heights above 750 m at 1845. Both regions of strong (> 12.5 m s^{-1}) outflow on either side of the microburst are shallow, with the southeastern side appearing to have strong winds that are somewhat deeper than those on the northwest.

In these and all subsequent vertical cross sections, the strongest winds appear at the surface. This is an artifact of the averaging performed within the radar beam, and the fact that winds representative of those at 30 to 100 m above the surface are placed on the 0.0

9
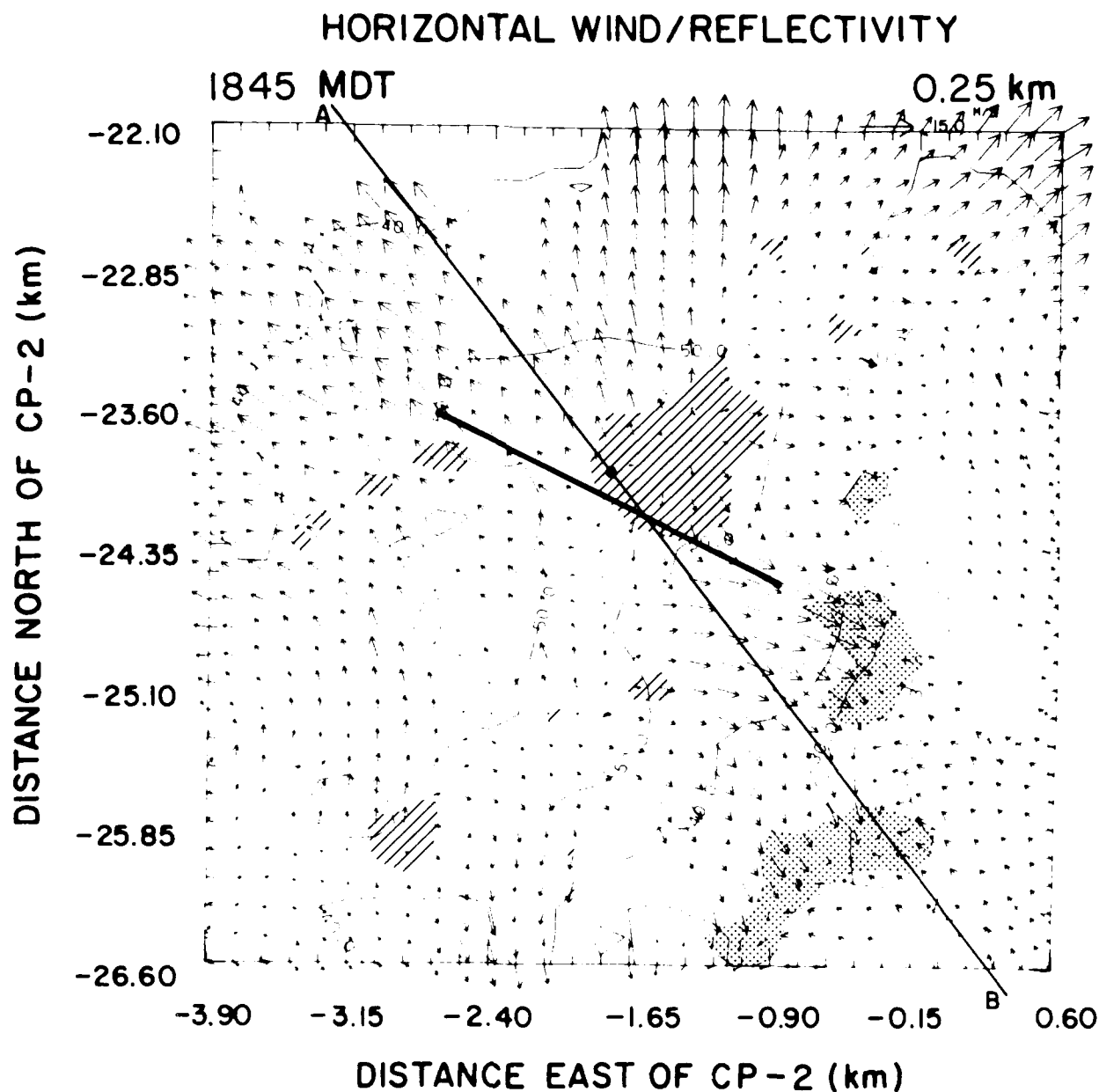
FIGURE 3B. 1845 MDT analyzed horizontal wind vectors at 0.25 km height overlaid by reflectivity. Also shown is vertical velocity. Downdrafts shown by hatching, updrafts by stippling. Hatching shows areas of $w < -5$ m s^{-1}; cross hatching shows $w < -10$ m s^{-1} (not shown in this figure). Maximum $\frac{\Delta V}{\Delta r}$ shown by short solid line, path AB shown by labeled solid line.

10
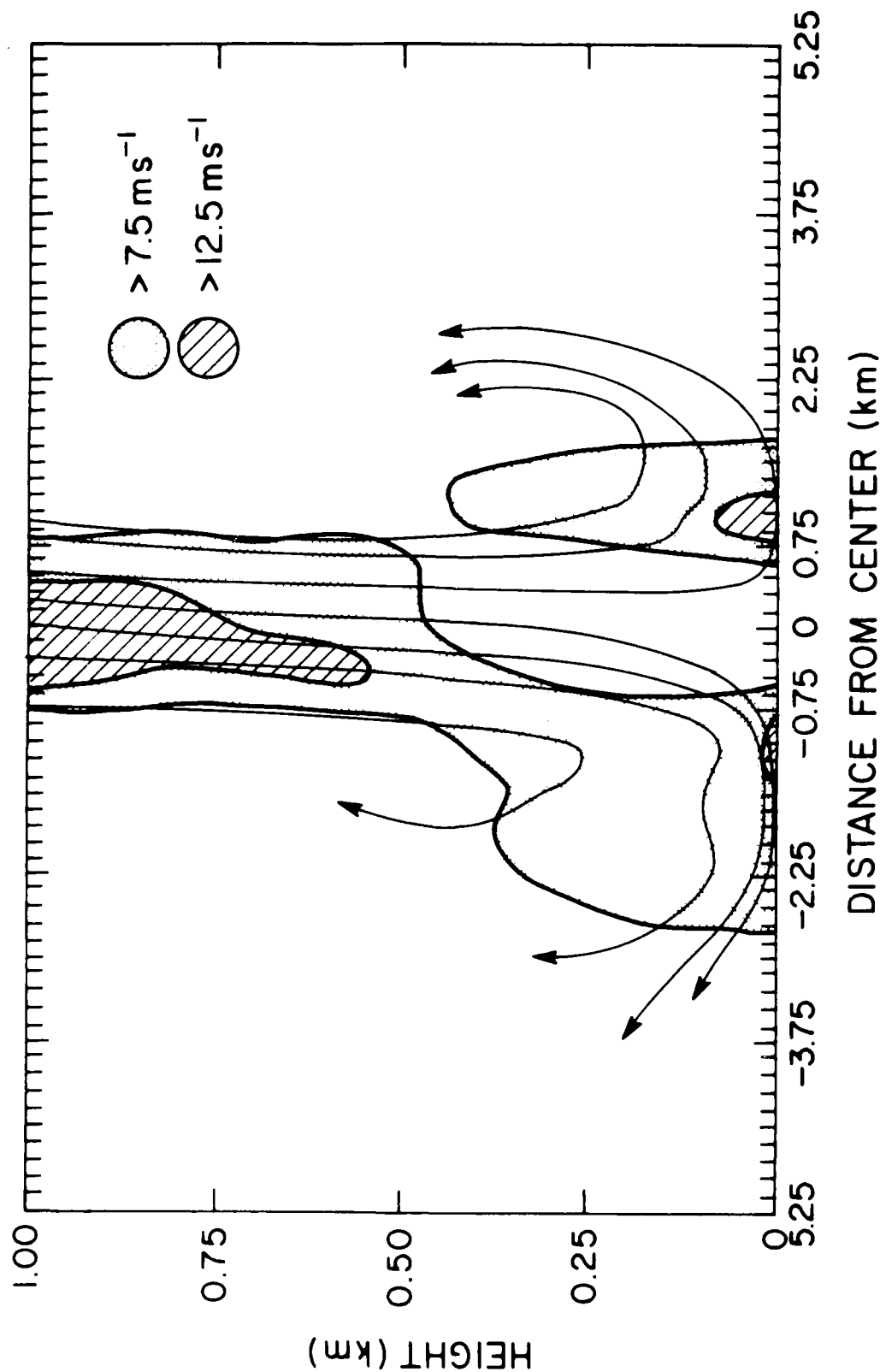
FIGURE 3C. Schematic northwest to southeast vertical cross section through the lowest 1 km of the microburst at 1845 MDT. Streamlines represent a composite of several cross sections near the microburst center. Stippling shows wind speeds 7.5 m s⁻¹ and greater, hatching shows wind speeds 12.0 m s⁻¹ and greater. Tic marks every 150 m horizontally, 250 m vertically.

11

km grid level. In fact, winds at the surface will be somewhat weaker than those shown, while the maximum winds above the surface will be somewhat stronger (Kessinger *et al.*, 1983).

c. 1847 Analysis Time

Figure 4a shows the 0.0 km analysis level roughly 2 min later. This is the time of maximum intensity for this microburst. Reflectivity has increased to nearly 58 dBZ$_e$ at the 0.0 km grid level, and the maximum vector velocity change has increased to 32 m s^{-1} over the path shown (the other paths are discussed later). The distance over which this vector difference occurs has increased to 2.3 km, in accord with an overall expansion of the microburst outflow. Thus, the average shear intensity over the bold line is now $14 \cdot 10^{-3}$ s^{-1}.

Downdraft intensity has also increased markedly, to a maximum of 13 m s^{-1} at the 250 m grid level (Fig. 4b). The horizontal extent of downdraft stronger than 5 m s^{-1} has decreased slightly; its approximate diameter is between 0.75 and 1.0 km. By this time the downdraft appears more circular yet the outflow is still asymmetric.

At 0.25 km the maximum vector velocity difference has increased to 28 m s^{-1} over 2.6 km along the indicated path but yielding a lower average shear ($11 \cdot 10^{-3}$ s^{-1}). The horizontal extent of the outflow changes little with height over the lowest 250 m of the analysis. Maximum reflectivity associated with the microburst at 250 m is equivalent to the reflectivity at the lowest grid level.

Figure 4c shows the microburst in vertical cross section. The downdraft has strengthened considerably, with strong downdraft evident as low as 350 to 400 m above the surface. The region of strong outflow wind has deepened considerably on the southeast side, with horizontal winds stronger than 12.5 m s^{-1} extending well above 250 m. The horizontal extent of strong winds near the surface has also increased somewhat. Strong winds on the northwest side have deepened slightly, but these are still weaker and shallower than their counterparts to the southeast. The northwest curl has weakened. Note the stagnation region directly under the microburst center.

d. 1850 Analysis Time

By 1850 the microburst has a noticeably different appearance from the previous analyses. In general the outflow structure does not appear as well defined while the southeast velocity maximum appears to be propagating outward somewhat independently of the central structure. There is a noticeable area of calm winds near the microburst center. Although the maximum average shear across the microburst has decreased, two areas of relatively strong shear exist on either side, associated with the local velocity maxima centered near (0.15, 24.50) and (3.60, 23.60).

Figure 5a shows wind field vectors and reflectivity at the 0.0 km level. The maximum vector velocity difference across the microburst is maintained at 33 m s^{-1}. However, the magnitude of shear is reduced to an average of $11 \cdot 10^{-3}$ s^{-1} because of lateral spreading to
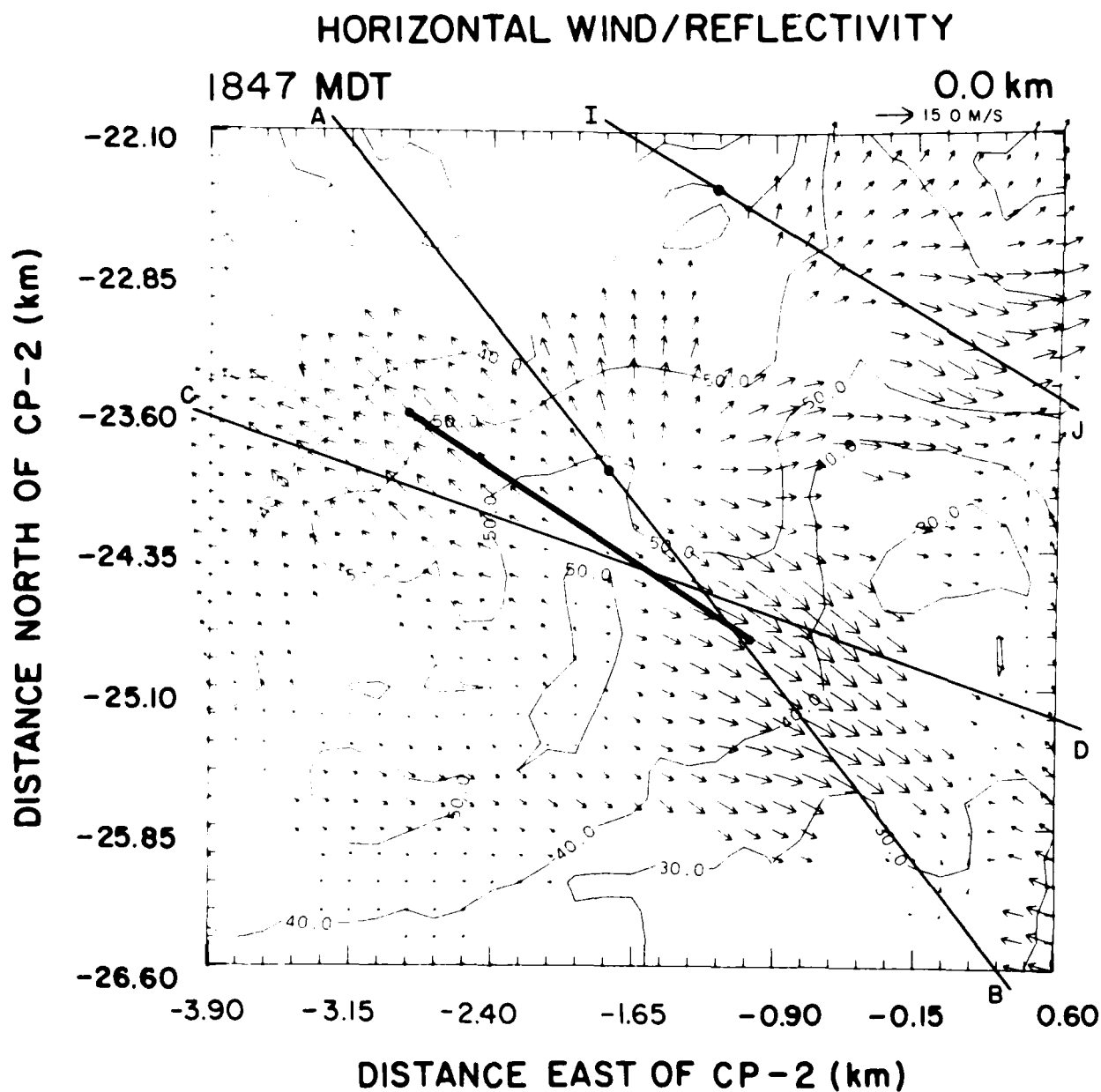
FIGURE 4A. 1847 MDT analyzed horizontal wind and reflectivity at 0.0 km. In addition to path AB and the maximum $\frac{\Delta V}{\Delta r}$ at 0.0 and 0.25 km, paths CD and IJ are shown, similar to 3a.

13
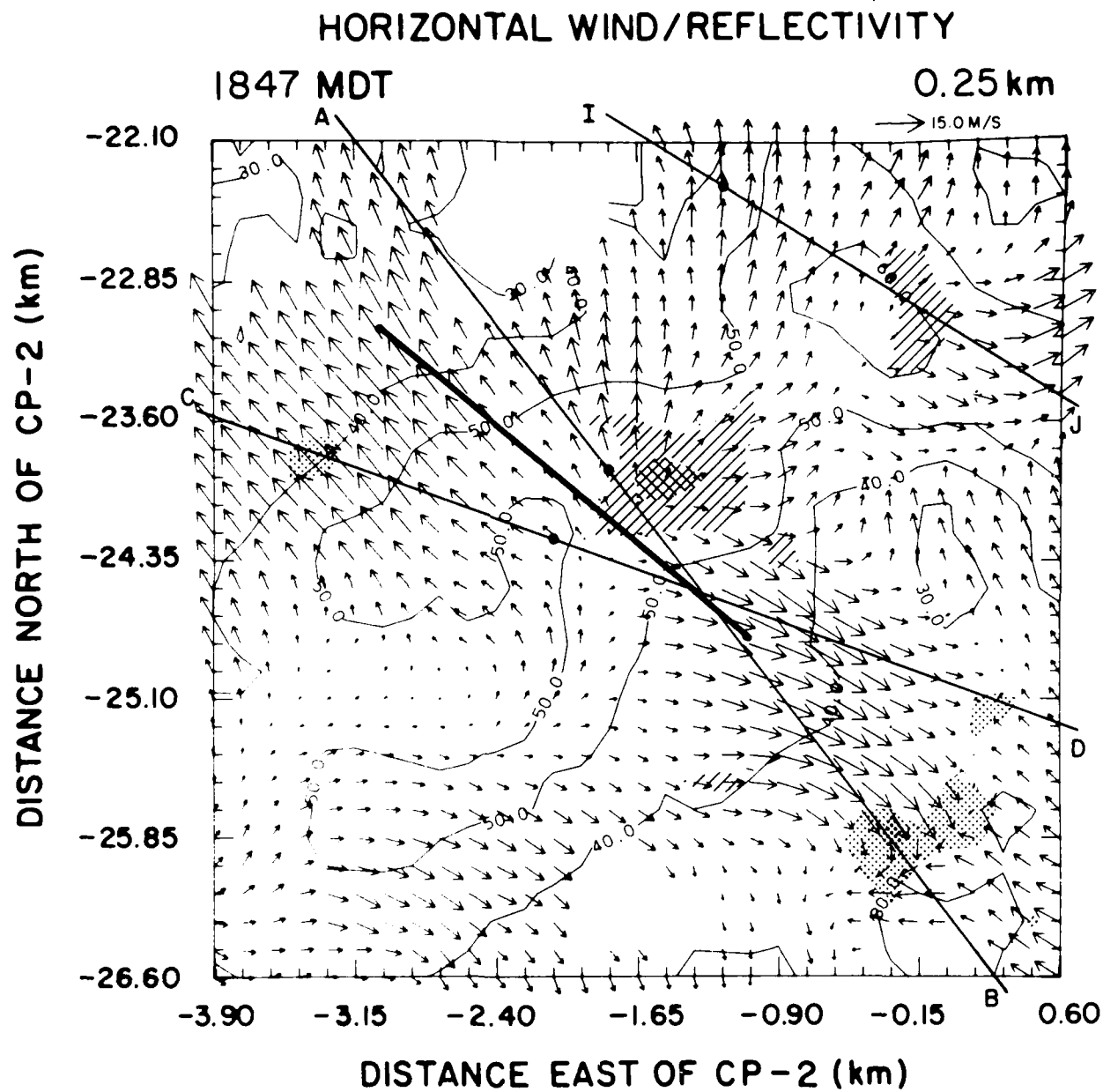
FIGURE 4B. 1847 MDT analyzed horizontal wind and reflectivity with maximum $\frac{\Delta V_t}{\Delta r}$. Paths AB, CD, and IJ are shown, similar to 3c.

14

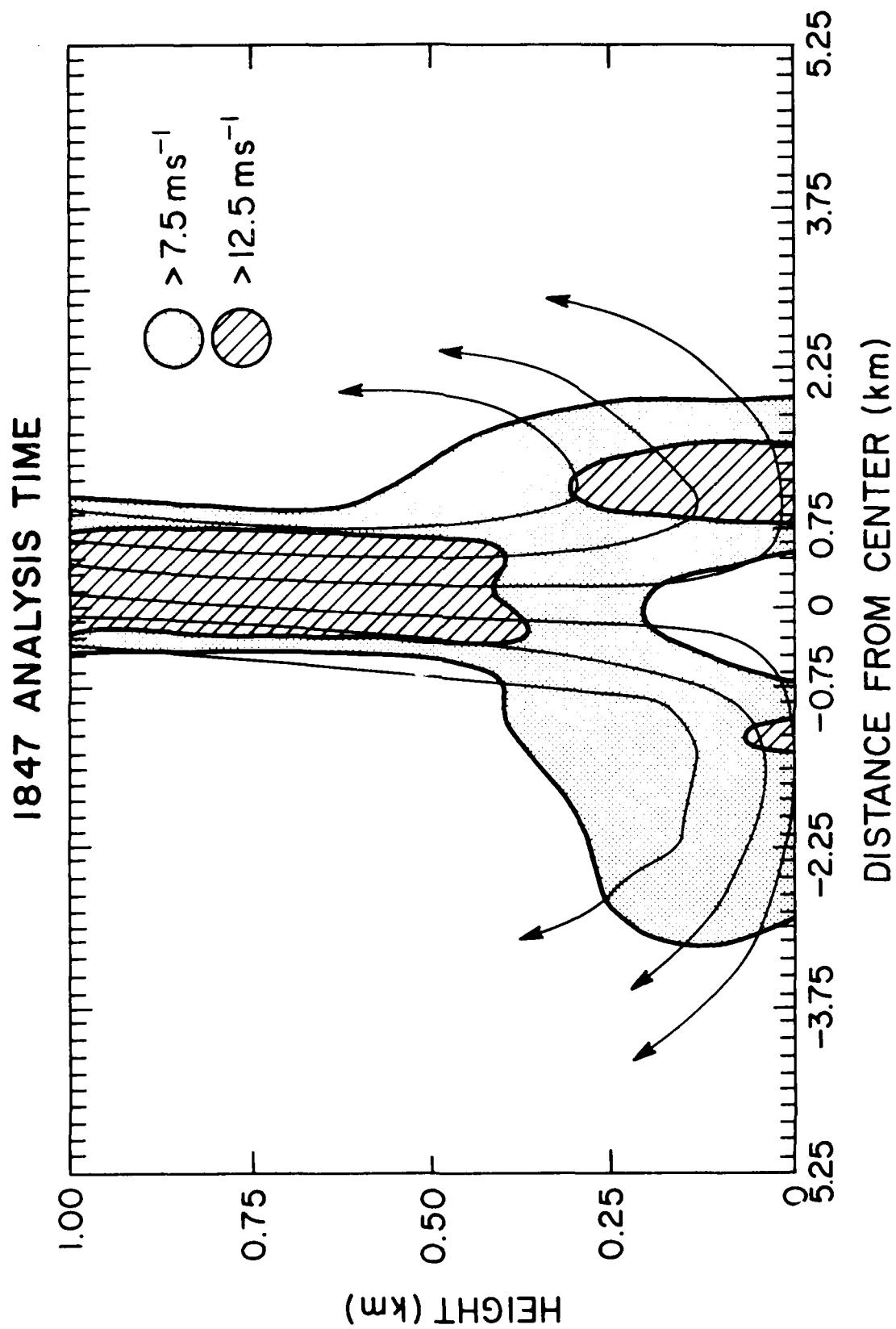FIGURE 4C. Schematic northwest-southeast oriented vertical cross section through the lowest 1 km of the 1847 MDT analysis, similar to 3d.

15

FIGURE 5A 1850 MDT analyzed horizontal wind and reflectivity at 0.0 km, showing the maximum path and path AB, similar to previous figures.

16

3.0 km distance. The increase in horizontal extent stems almost entirely from an expansion of the outflow towards the southeast. The maximum reflectivity remains stable at 57 dBZ_e.

In Fig. 5b, downdraft intensity is only half that in the 1847 analysis, with a maximum strength of between 8 and 9 m s^{-1}. Horizontal extent of downdraft stronger than 5 m s^{-1} is difficult to determine as the downdraft has become quite elongated in the northwest-southeast direction (1.3 km long and only 0.3 km wide). However, the central downdraft is clearly less organized and appears considerably weaker.

At this level, the maximum vector velocity difference across the microburst is 30 m s^{-1} over a 2.8 km distance yielding 11×10^{-3} s^{-1} average shear. This is in contrast to the previous two analyses, where the vector differential across the microburst was weaker at the 250 m grid level than at the 0 m grid level over a slightly larger distance. Maximum reflectivity at this level is 59 dBZ_e, up from the previous analysis.

Figure 5c shows that the outflow on the southeast side has decreased dramatically, with no significant region of winds stronger than 12.5 m s^{-1}. The strongest downdraft region has shifted towards the northwest. The downdraft no longer covers as large a horizontal area and does not appear as close to the surface as before. In concert with the northwestward shift of the downdraft, the strong horizontal winds on the northwest side have deepened and expanded. The northwest curl has not changed appreciably since the previous analysis.

e. 1852 Analysis Time

Figure 6a shows the wind field and reflectivity for 1852 at the 0.0 km level. The microburst outflow structure is weaker and less organized. Maximum vector wind difference across it is down to 25 m s^{-1} over a distance of 2.6 km (average shear of $9.8 \cdot 10^{-3}$ s^{-1}) while the maximum analyzed radar reflectivity at this level is 57 dBZ_e. The wind maximum on the southeast side is much weaker.

As shown in Fig. 6b, the downdraft no longer has a distinct core. Maximum downdraft velocity near the center has decreased to 6 m s^{-1}. To the southwest there is an isolated downdraft core of nearly 10 m s^{-1}. This may explain the persistence and apparent lack of movement of the northwest wind maximum, i.e., there is an imbedded microburst in its earliest stages of development.

Figure 6b shows further evidence of microburst dissipation in the analyzed horizontal winds, which have weakened even further and have become somewhat more disorganized. The maximum vector differential across the microburst at 250 m is 23 m s^{-1} over 2.8 km (mean shear of $8 \cdot 10^{-3}$ s^{-1}), substantially weaker than the 1850 analysis. Even though it has weakened considerably, this microburst could still pose a hazard to jet transport aircraft. Maximum reflectivity is still above 58 dBZ_e.

Figure 6c clearly shows the microburst well into its dissipation stage. There are no significant areas of horizontal winds stronger than 7.5 m s^{-1} on the southeast side, and the strong winds on the northwest side are nearly gone. Downdraft stronger than 12.5

17

FIGURE 5B 1850 MDT analyzed horizontal and reflectivity at 0.25 km, similar to previous figures.

FIGURE 5C. Schematic northwest-southeast oriented vertical cross section through the lowest 1 km of the 1850 MDT analysis, similar to previous figures.
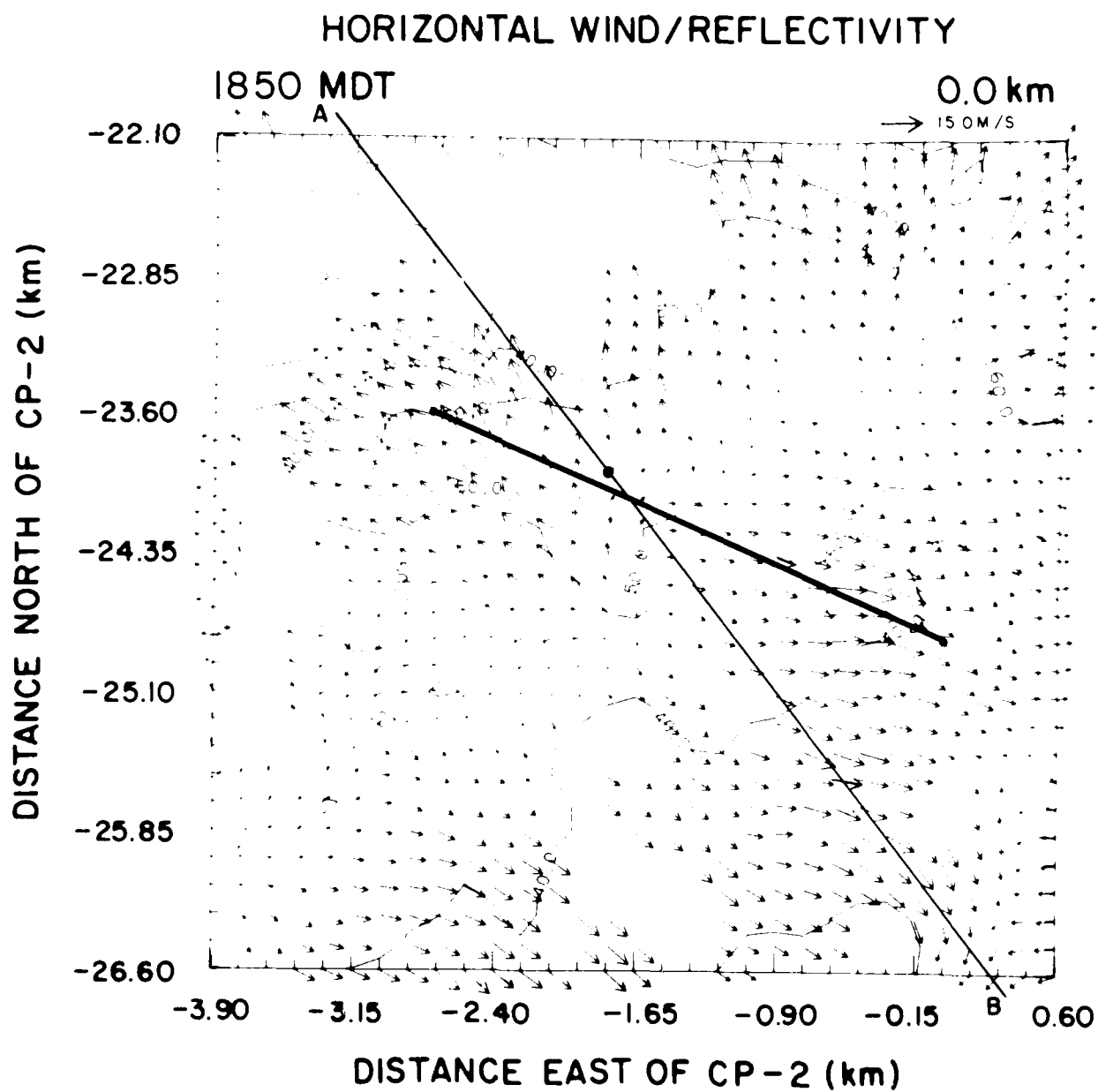
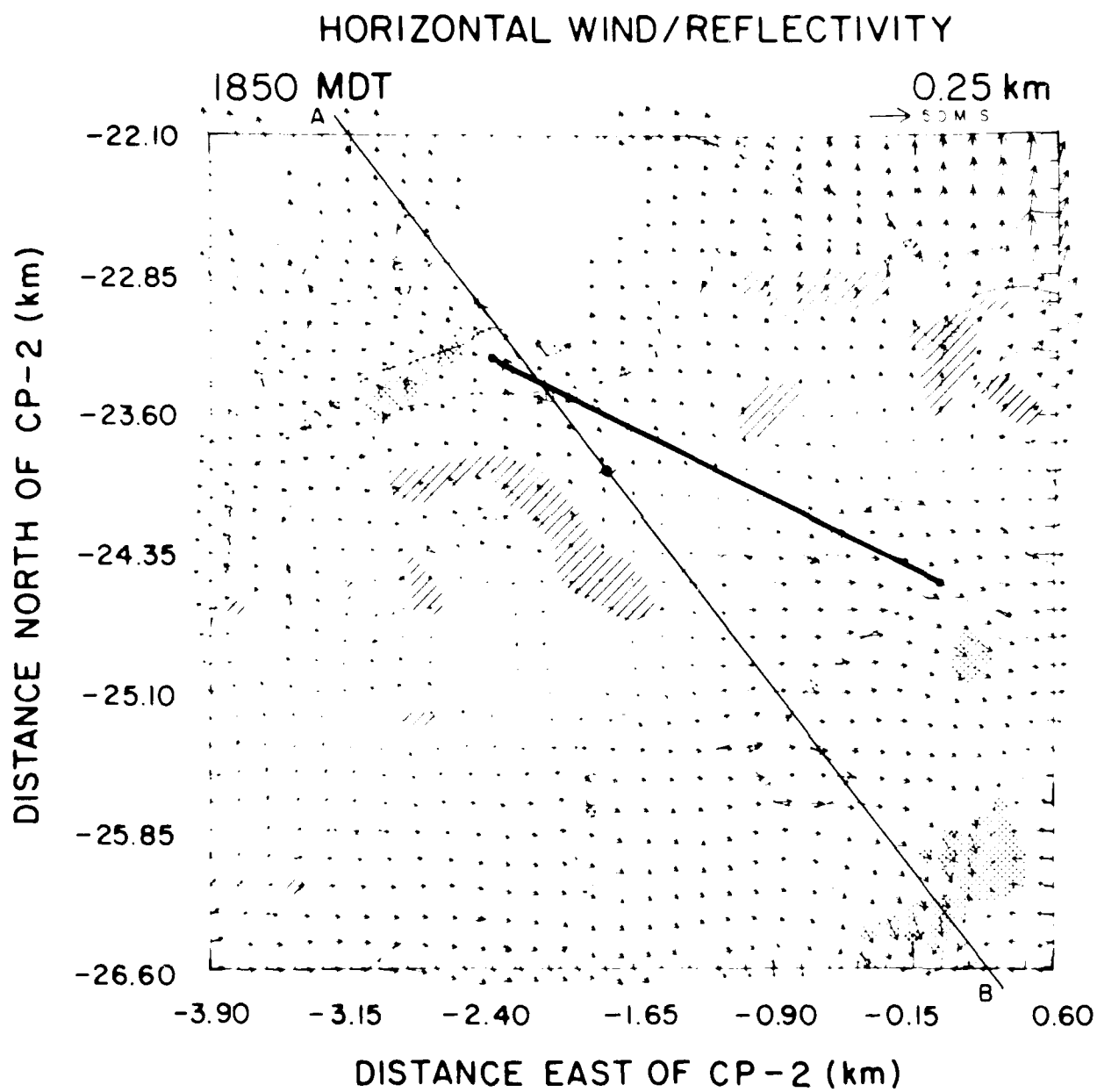FIGURE 6A. 1852 MDT analyzed horizontal winds and reflectivity similar to previous figures.

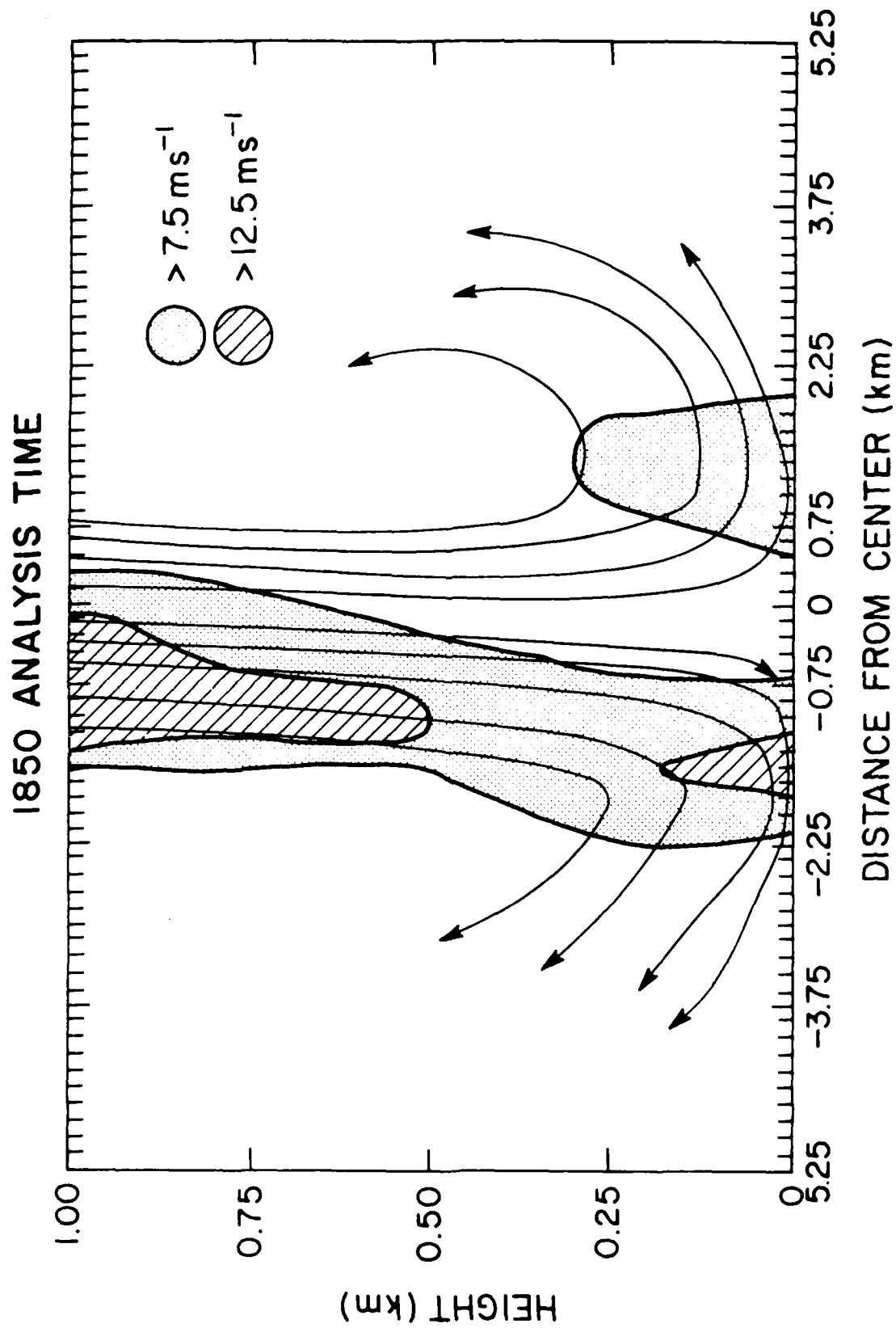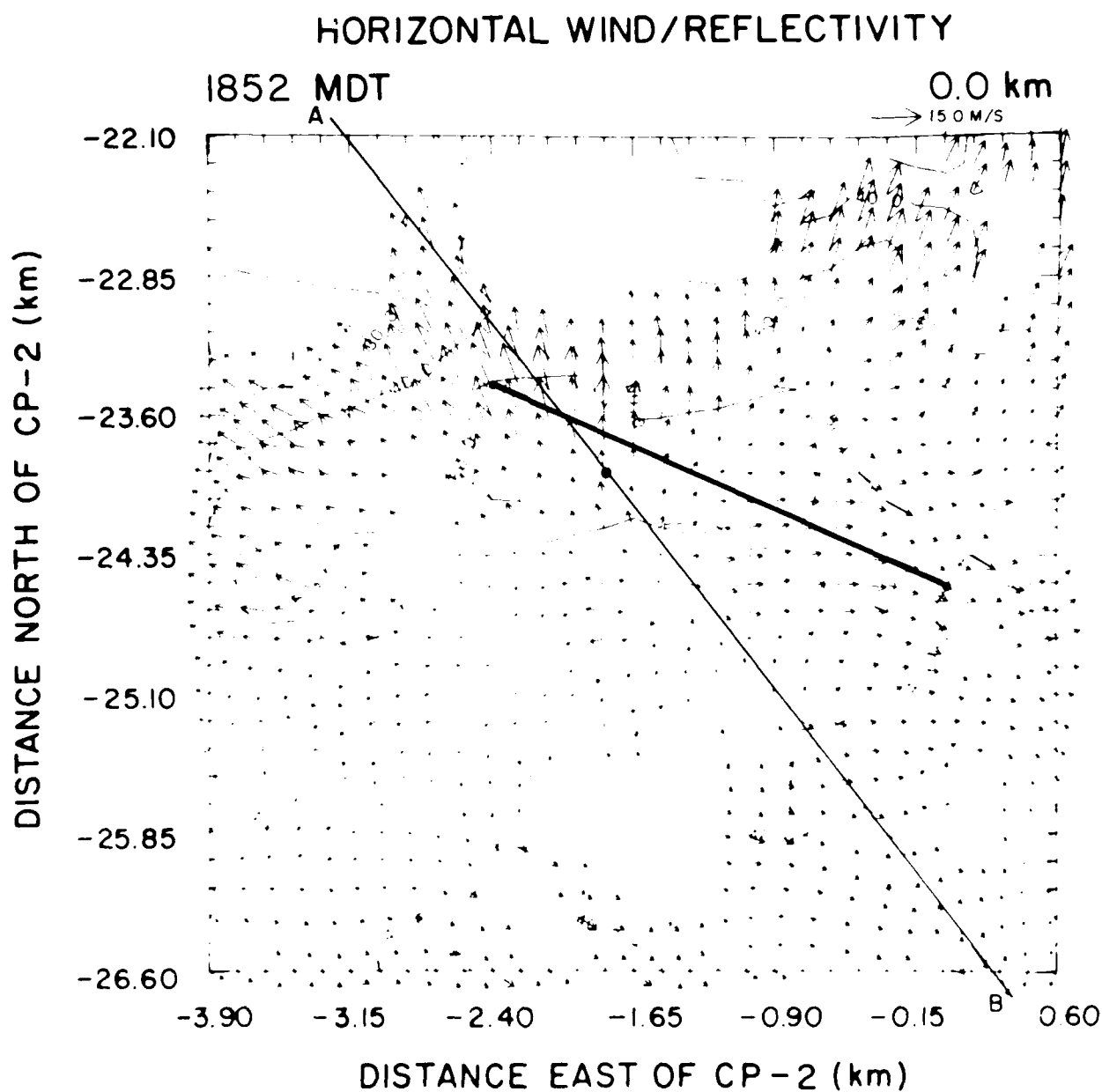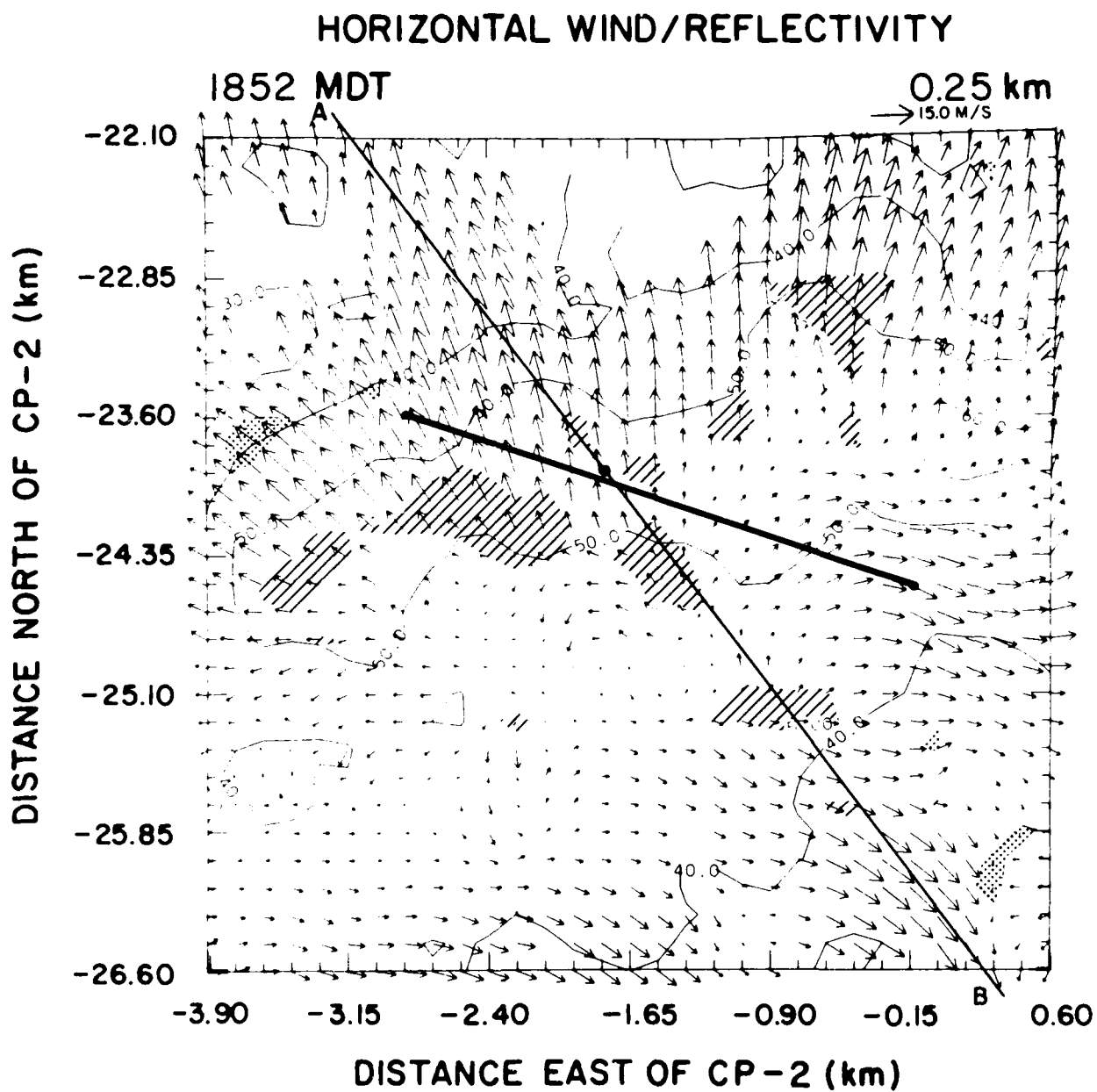FIGURE 6B. 1852 MDT analyzed horizontal winds and reflectivity, similar to previous figures.

21
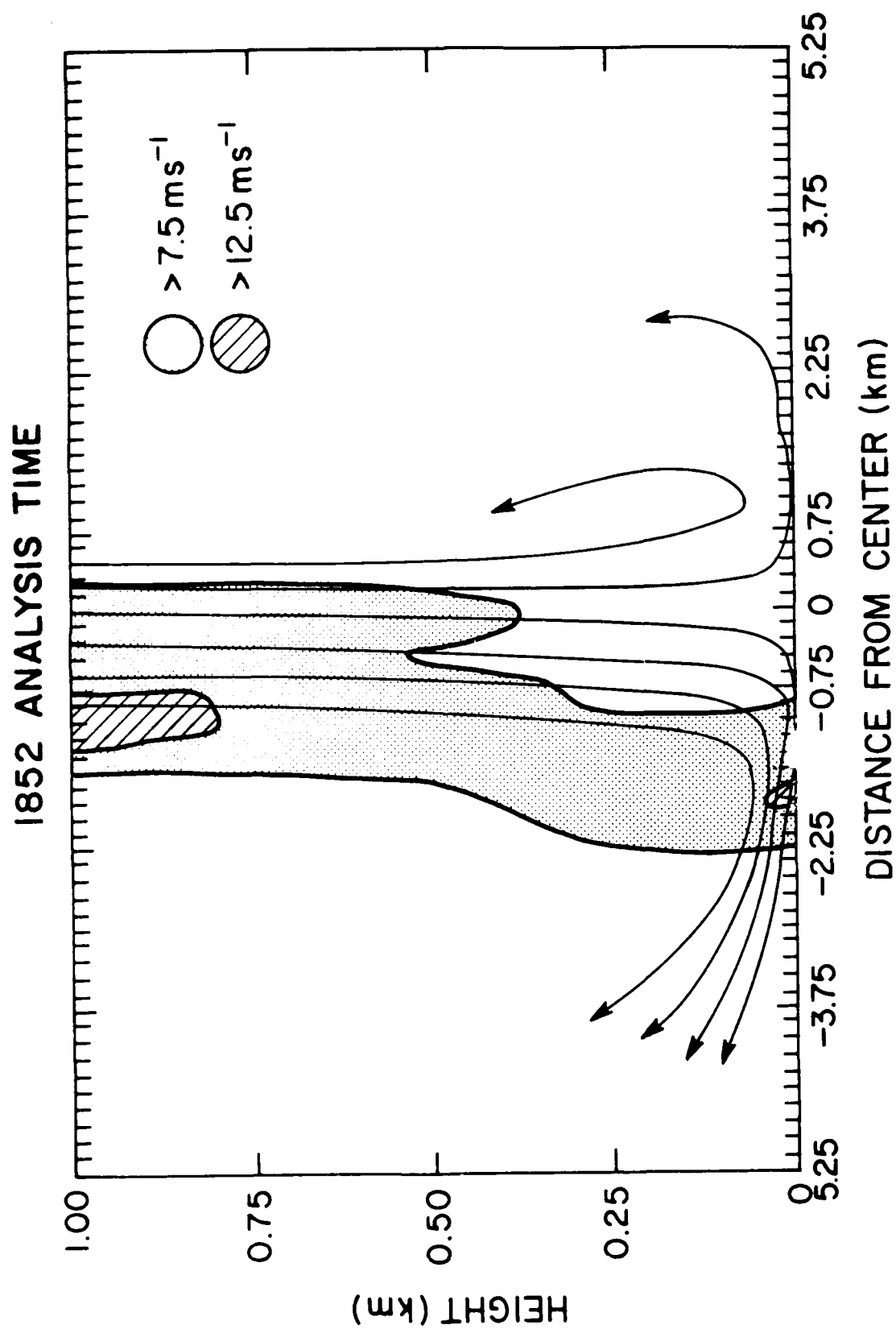
FIGURE 6C. Schematic northwest-southeast oriented cross section through the lowest 1 km of the 1852 MDT analysis, similar to previous figures.

22

m s^{-1} extends to only slightly above the 750 m level and has shrunk in horizontal extent even further. Also, the curl on the northwest side has nearly dissipated.

f. Missing Data

All previous figures contain data void regions due to ground-clutter contamination. For purposes of numerical modeling and flight simulation it is necessary to estimate flow field values in these intervening regions. For the same reason the first grid level was placed at 0.0 km rather than a more strictly correct 0.06 km.

Leise (1981) developed a data extension technique performing either interpolation or, when necessary, extrapolation. The extension method is an averaging technique that approaches the sample mean as distance from the actual data increases.

Interpolation and extrapolation is performed in three dimensions only on u and v. After computing a new divergence field from the new u and v fields, divergence is integrated upward from a surface boundary condition of $w = 0$. Since this technique does not modify any preexisting data, vertical velocity in areas containing data at the surface remain unaltered by the processing.

This method is a solution to Poisson's equation when the data void region is surrounded by good data. If not, the method is linear. When extrapolating, the method converges to the sample mean as distance from the data increases, ensuring numerical stability. Finally, no interpolated or extrapolated value can exceed the dynamic range of the original data; extended values are always greater than the minimum and less than the maximum. Figure 7 shows wind vectors at the 0.0 km level of the 1847 MDT analysis after filling. Comparison to Fig. 4a, showing the wind vectors before filling, shows that the fill procedure altered none of the preexisting winds.

3. Flight Simulation Results

a. The Numerical Aircraft Model

The aircraft model (hereafter refered to as "model") evaluates the first and second derivatives of all three components of motion (longitudinal, latitudinal, and vertical) and so has six degrees of freedom. Full details of this model can be found in Frost *et al.* (1985), Frost and Bowles (1984), and Turkel *et al.* (1981). This model possesses some gross characteristics of Boeing 727 aircraft in service, *i.e.*, maximum landing and takeoff weights, total available thrust, and flap settings during approach and departure, but is not a rigorous model of a Boeing 727 aircraft. The Boeing 727 series is one of the most common air carrier jet aircraft currently in service and so suffers the highest collective probability of a microburst encounter.

A "pilot" is included, *i.e.*, a set of control laws (Turkel *et al.*, 1981) are used to maintain a 3° approach path vertically and proper horizontal ground track, by adjusting pitch, roll, yaw, and thrust. During the departure climb, the control instructions attempt first to maintain a constant pitch angle and second, to maintain a target airspeed. These control laws include suitable delays in pilot reactions ($\approx$ 2 s, depending on the parameter) and

23

HORIZONTAL WIND/REFLECTIVITY

FIGURE 7. 1847 MDT analyzed horizontal wind after filling missing data using the Liese technique, overlaid with reflectivity. Paths AB, CD, and IJ are shown, as in 4a.

commanded thrust responses, meaning the pilot does not respond instantly to approach path changes and engines do not supply thrust instantly upon demand. All approaches and depa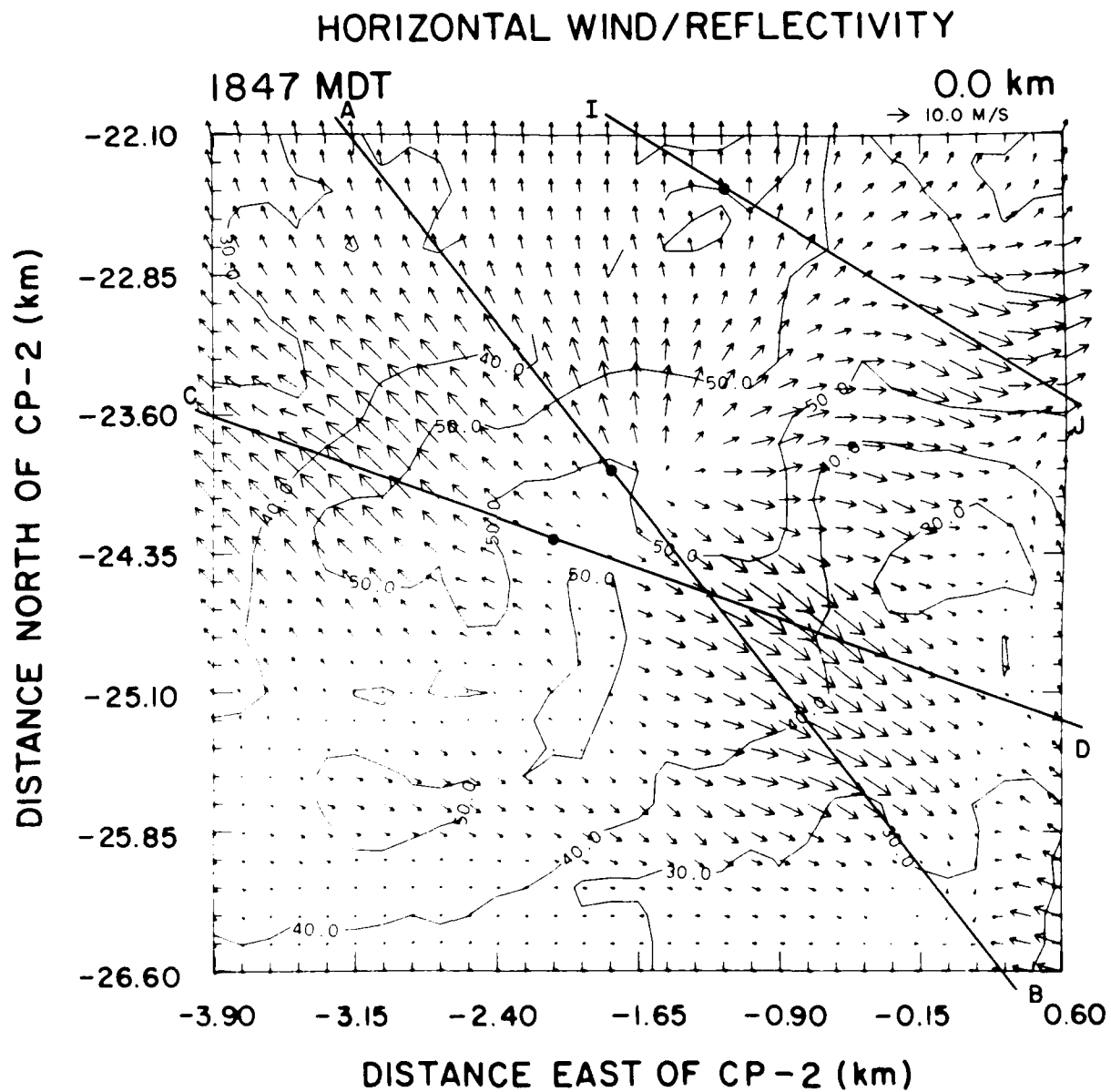rtures are standard, using no special energy trade flight techniques. Consequently, all aircraft/pilot responses are underestimated in light of some energy trade procedures that can be used, *i.e.*, trading kinetic energy (airspeed) for potential energy (altitude).

Prior to entering the simulated wind shear, the model determines aircraft trim using the winds that would be first encountered on an undisturbed 3° approach path projection into the data. As the aircraft proceeds, wind components along the path are interpolated using a three-dimensional, linear, volume-weighted scheme (Frost *et al.*, 1985). Adding a fourth dimension (time) to the interpolator allows representation of winds in a Lagrangian reference frame.

b. Wind Shear Classification

If the model remains exactly on the desired approach (or departure) path, it will pass through some point defined by the the distance east (x_{ref}), north (y_{ref}), and above (z_{ref}) the origin. The approach criteria call for the aircraft to attempt a go-around if it deviates outside a 0.7° cone around the desired approach path. These criteria are somewhat less severe (in the allowable vertical deviation) than most go-around thresholds used operationally, e.g., 0.25°. A go-around consists of full thrust (about 10% above the operationally used "rated takeoff thrust") and a 15° pitch up command.

Using the above, three difficulty classifications are defined describing the wind shear along each flight path. A case is classified as Class I (most difficult) if a go-around attempt, which by definition occurs during an approach, fails. A Class I departure case results if the aircraft contacts the ground after liftoff or suffers such reduced performance that obstructions commonly found around airports cannot be cleared, e.g., a 15 m tree 1 km from the liftoff point. An approach is Class II (moderate difficulty) if a go-around is successful. For departure, Class II indicates that climb performance is noticeably degraded. Finally, if the aircraft never passes outside the 0.7°cone during approach the wind shear is classified as Class III (minimal difficulty). Similarly, a Class III departure case results in a somewhat longer takeoff roll than usual, an inconsequential decrease in climb performance, or both.

These results are, by their nature, aircraft dependent. One aircraft pilot combination may be capable of successfully negotiating a given path through the microburst while another may not. Thus, these classifications have strict meaning only for the particular numerical model and control laws used; actual results in manned simulators or real aircraft will depend on many factors such as aircraft type and pilot awareness. These results are intended as a guide in determining how much difficulty a particular path may pose to an aircraft. Lastly, all modelled results use standard sea level atmospheric conditions even though the data were gathered near Denver, 1.6 km above sea level. If altitude were considered here, the performance capability of the model would be somewhat reduced.

In the following, simulated approaches along two nearby paths are examined to understand how the three-dimensional microburst wind field affects the model. Next, approaches

along the same path at different analysis times are performed to understand how temporal changes in the microburst affect the model. Finally, departures are examined to understand how the microburst affects departure performance along two nearby paths and how microburst location relative to liftoff point affects departure performance.

c. Approach Path Examples

Figure 7 shows the paths tested together with wind vectors and reflectivity contours at the 0.0 km level of the 1847 analysis. Figure 8 shows the coordinate system used to define an approach path. For all cases the flight path and the path of maximum mean horizontal shear do not coincide, because flight paths were chosen to reflect the overall microburst structure, including headwind, center of downdraft, and tailwind, rather than exclusively focusing on the maximum headwind to tailwind shear. Heavy dots show the reference points (x_{ref}, y_{ref}) that define each path while Table 2 lists the reference points and clockwise angles each path makes with respect to the x axis. Representative examples of Class I (most difficult) and Class II (moderately difficult) cases are shown, though many more paths than are shown were investigated.

Flight Path	Coordinates (x_{ref}, y_{ref}) of Corresponding Microburst Center on Each Path Relative to CP-2 (km).	Angle Clockwise From x-Axis
AB	(1.80, -23.90)	52.7
CD	(2.10, -24.28)	19.9°
IJ	(1.20, -22.40)	32.3°

Table 2. Investigated paths.

Figure 9a shows the modelled flight path on the wind component parallel to the vertical cross section, taken along path AB. This plot is similar to the schematic vertical cross sections shown previously. For all vertical cross sections, the distance scale across the bottom gives the along-path distance from the reference point, at zero on the distance scale and shown by the heavy vertical line. A dotted line shows the 3° approach path while two dashed lines on either side show the limits of the 0.7° cone; if the model crosses outside those limits, a go-around is initiated. Approach path AB takes the model over the reference point at a z_{ref} of 100 m. The heavy line shows the flight path taken by the model. For this and subsequent figures showing the parallel or along-path wind component, dashed (negative) contours indicate a relative headwind and solid (positive) contours indicate a relative tailwind, in m s^{-1}. At the bottom of Fig. 9a are graphs of the longitudinal wind that would be experienced by the model if it remained precisely on the 3° approach path (solid line) as well as the longitudinal shear (dashed line). The model never deviates significantly from the desired path (compared to the data resolution), so those winds are representative of what the model experiences. Positive longitudinal wind indicates performance decreasing headwind-to-tailwind shear requiring positive inertial
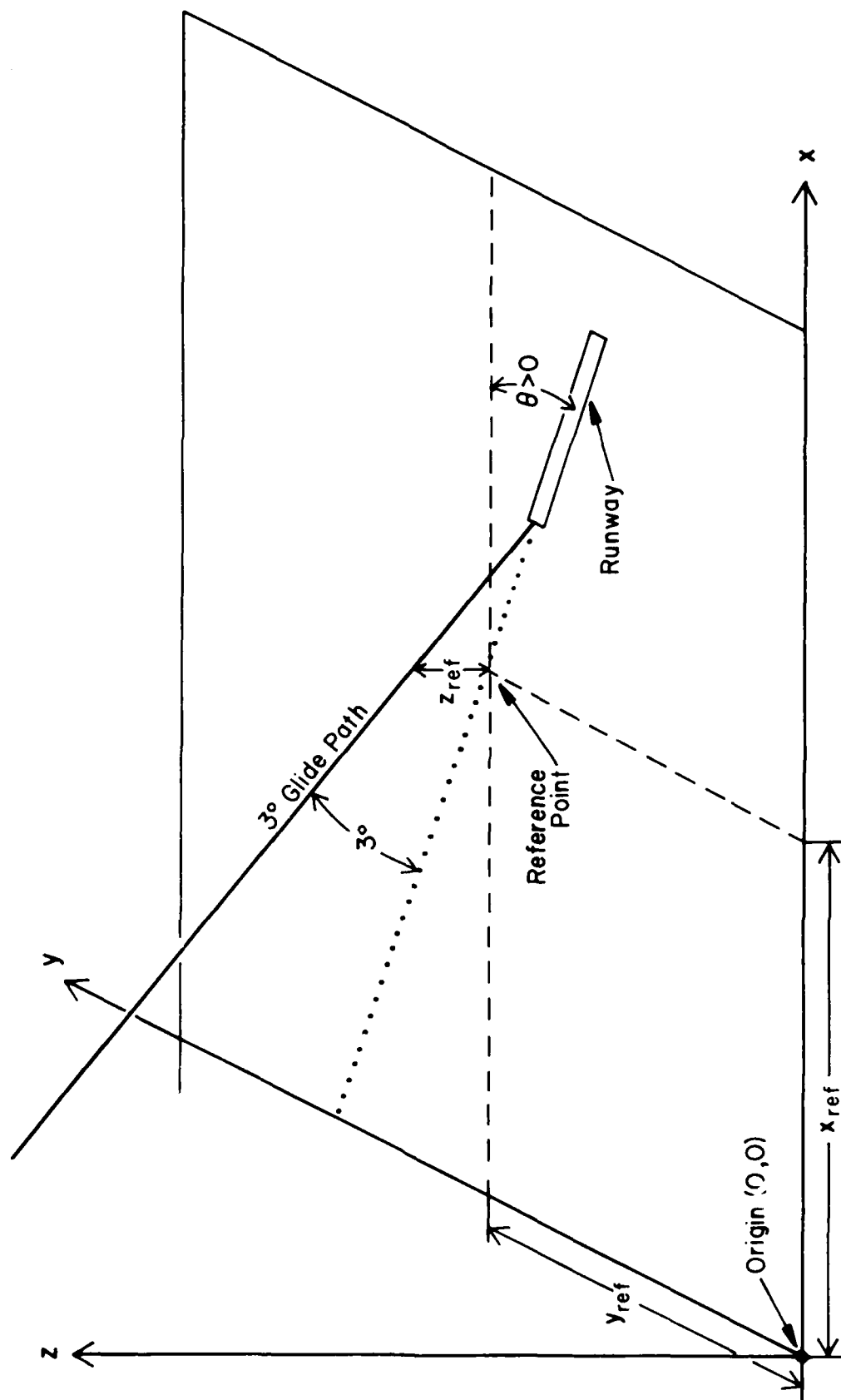
FIGURE 8. Coordinate system used to define approach paths. θ is positive clockwise; by this convention the approach path takes aircraft over (x_{ref}, y_{ref}) at height z_{ref}.

27
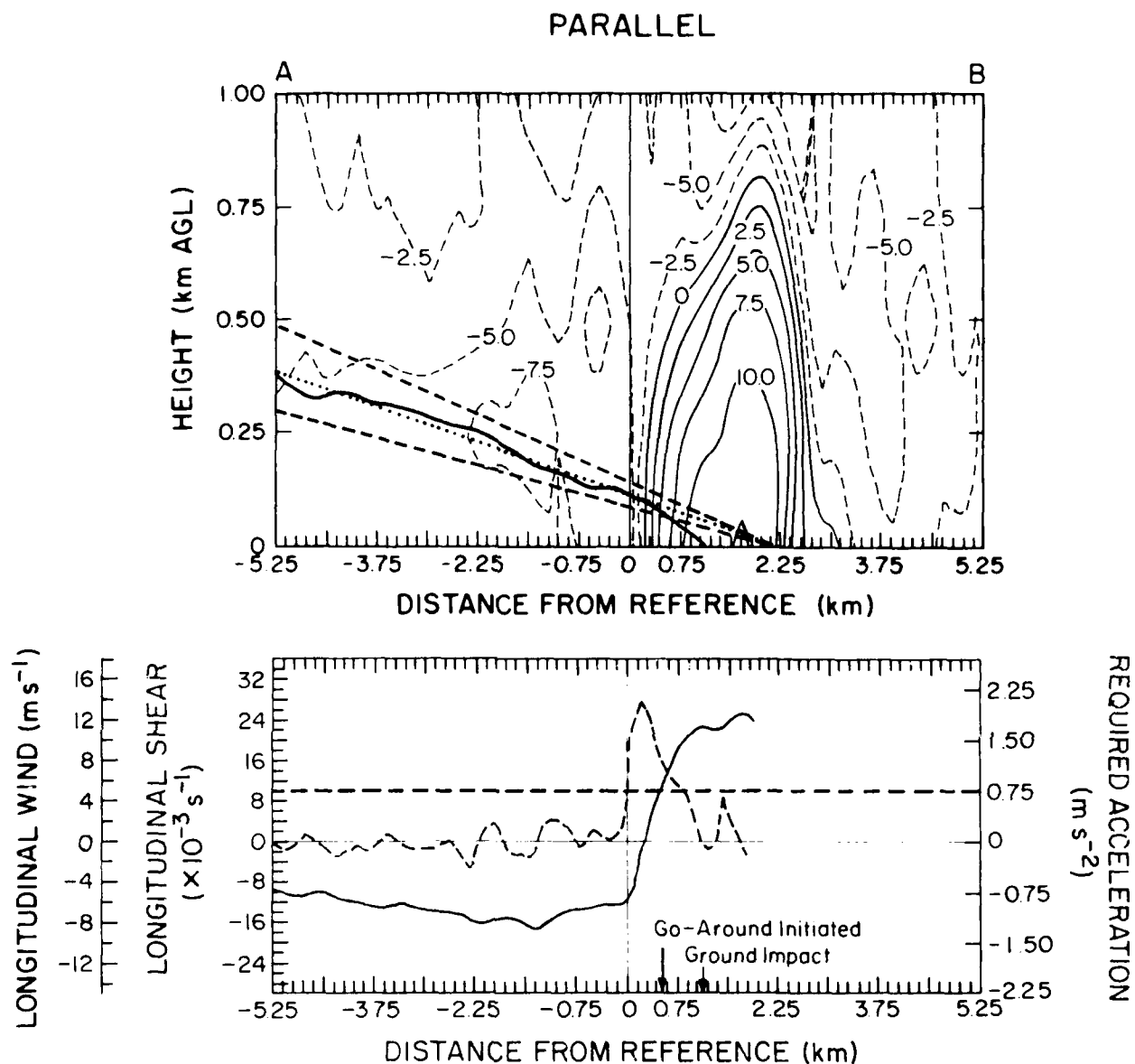
PARALLEL

FIGURE 9A. Modelled flight path along AB at 1847 plotted on vertical cross section of winds parallel to path, illustrating a Class I case. Contours in 2.5 m s⁻¹ increments; positive values indicate tailwind while negative values indicate headwind. Three-degree approach path shown by dotted line; 0.7° go-around thresholds shown by dashed lines. Center of cross section is at (x_{ref}, y_{ref}). Graphs below cross section show longitudinal wind (solid line), wind shear or required acceleration to maintain constant 75 m s⁻¹ airspeed (light dashed line), in m s⁻¹, s⁻¹ and m s⁻² respectively, that model would experience if it remained on the 3° glide slope shown. Heavy dashed line at 10×10^{-3} s⁻¹ shear value (0.75 m s⁻² required acceleration value) shows approximate maximum in-flight acceleration model is capable of. Significant points during simulated approach are shown.

28

acceleration, while negative shear indicates performance increasing tailwind-to-headwind shear. "Required acceleration" shows the longitudinal acceleration that would be required to maintain a constant airspeed of 75 m s^{-1}. This is computed by multiplying penetration airspeed by longitudinal shear. Positive values indicate inertial acceleration and negative values indicate inertial deceleration. The dashed line at 0.75 m s^{-2} required acceleration (10×10^{-3} s^{-1} shear) marks the maximum in-flight acceleration the model can attain. Any shears exceeding 10×10^{-3} s^{-1} require more inertial acceleration than the model is capable of and result in overall loss of airspeed and reduced lift.

Figure 9b plots the modelled flight path on the vertical wind component. As the model approaches the 8.5 m s^{-1} maximum headwind at -1.35 km it has been slowly rising above the approach path due to the increasing headwind shear, while the control laws have been reducing thrust to both maintain the target airspeed and regain the approach path. The approach path is reacquired immediately prior to passing through the maximum headwind component. Until this time, updraft and downdraft velocities have remained small. As the model traverses the headwind maximum, it loses the headwind that has been adjusted for and enters a downdraft region. Due to the headwind loss and downdraft combination, the modelled flight path continually and increasingly goes below the approach path.

As the increasing tailwind region is penetrated, the performance capability of the modelled airplane/pilot system is quickly exceeded because the longitudinal wind gradient is much stronger on the tailwind side of the microburst than on the headwind side. This is expected from previous discussion of the 1847 analysis. The average shear value along this path is 7.1×10^{-3} s^{-1} over 3.0 km. Between -0.15 and 1.0 km the average shear is 15×10^{-3} s^{-1}, and the downdraft has a magnitude of 3 m s^{-1}. As a result, the modelled path descends rapidly away from the desired path, reaching the go-around threshold just after the maximum downdraft point, slightly before 0.75 km, with 70 m of altitude. Clearly, strong downdrafts are not needed to produce realistic results. It is important to recognize that vertical velocity and horizontal shear play individually minor roles; downdrafts substantially increase the descent rate induced by horizontal wind shear which, in turn, drastically increases the energy required to recover. Results by Frost et al. (1985) and Turkel et al. (1981) show that horizontal winds alone or downdrafts alone do not pose a serious problem to the modelled aircraft. For example, when only the horizontal winds from path AB of the 1847 analysis are used in an approach simulation, excursions from the intended flight path are not sufficient to cause a go-around. The combination of the two components – downdraft and horizontal shear – is of prime importance. Because of this synergistic association, it is not possible to determine, say, what percentage of the total deviation from the desired path is due to downdraft and what percentage is due to horizontal shear.

At the go-around point full thrust with 15° pitch is commanded. Because of the low airspeed (10 m s^{-1} below the reference speed), large tailwind, high descent rate (7 m s^{-1}, almost twice the calm-condition nominal descent rate of 4 m s^{-1}) and low altitude, recovery is impossible; ground impact occurs nearly 1 km short of the intended touchdown point. This simulation bears similarities to the EAL Flight 66 approach accident, representing a Class I case.
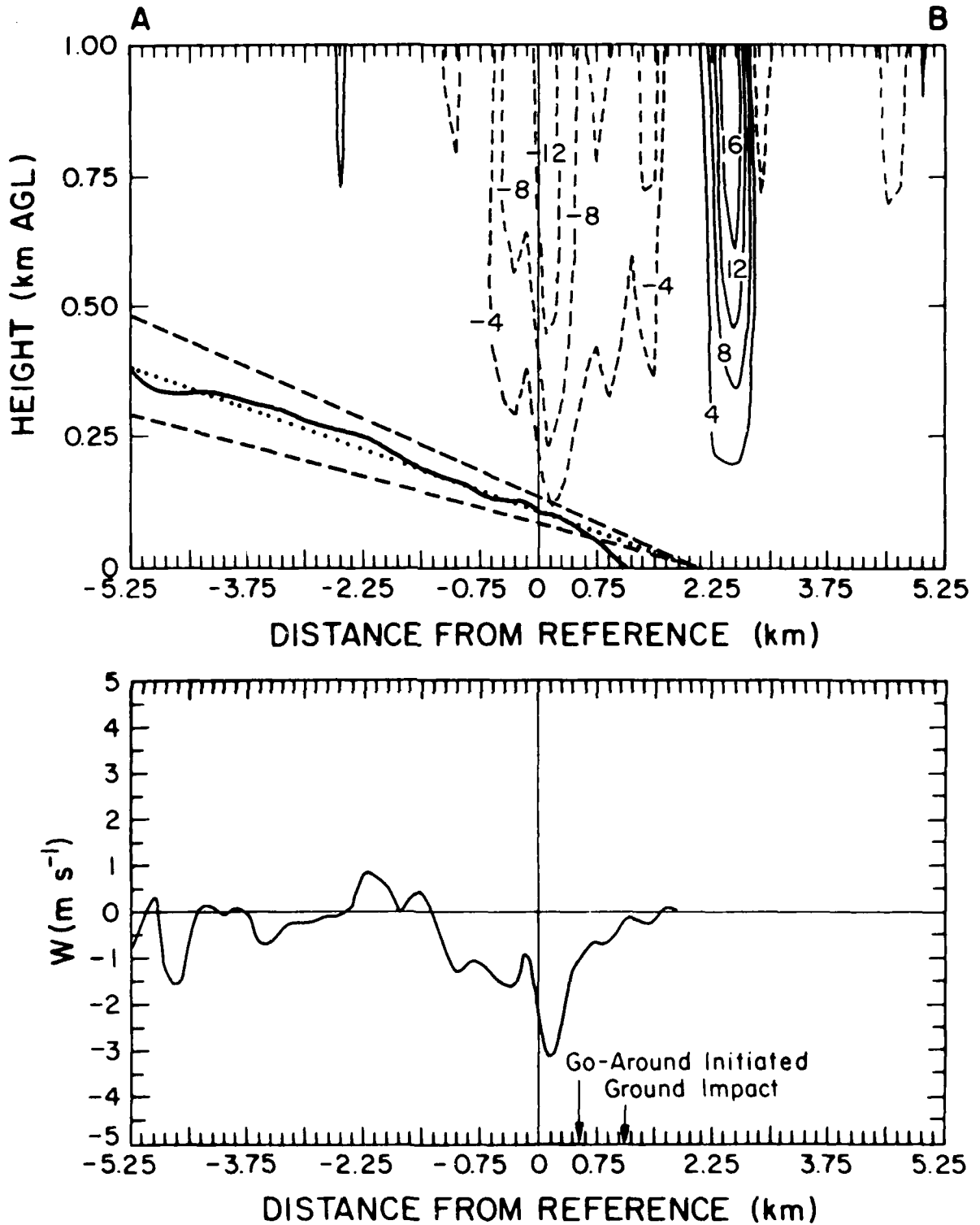
VERTICAL VELOCITY

FIGURE 9B. Similar to 9a, but for vertical wind, contoured in 4 m s^{-1} intervals. Graph at bottom shows vertical wind that would be experienced by model if it remained on the three degree approach path shown.
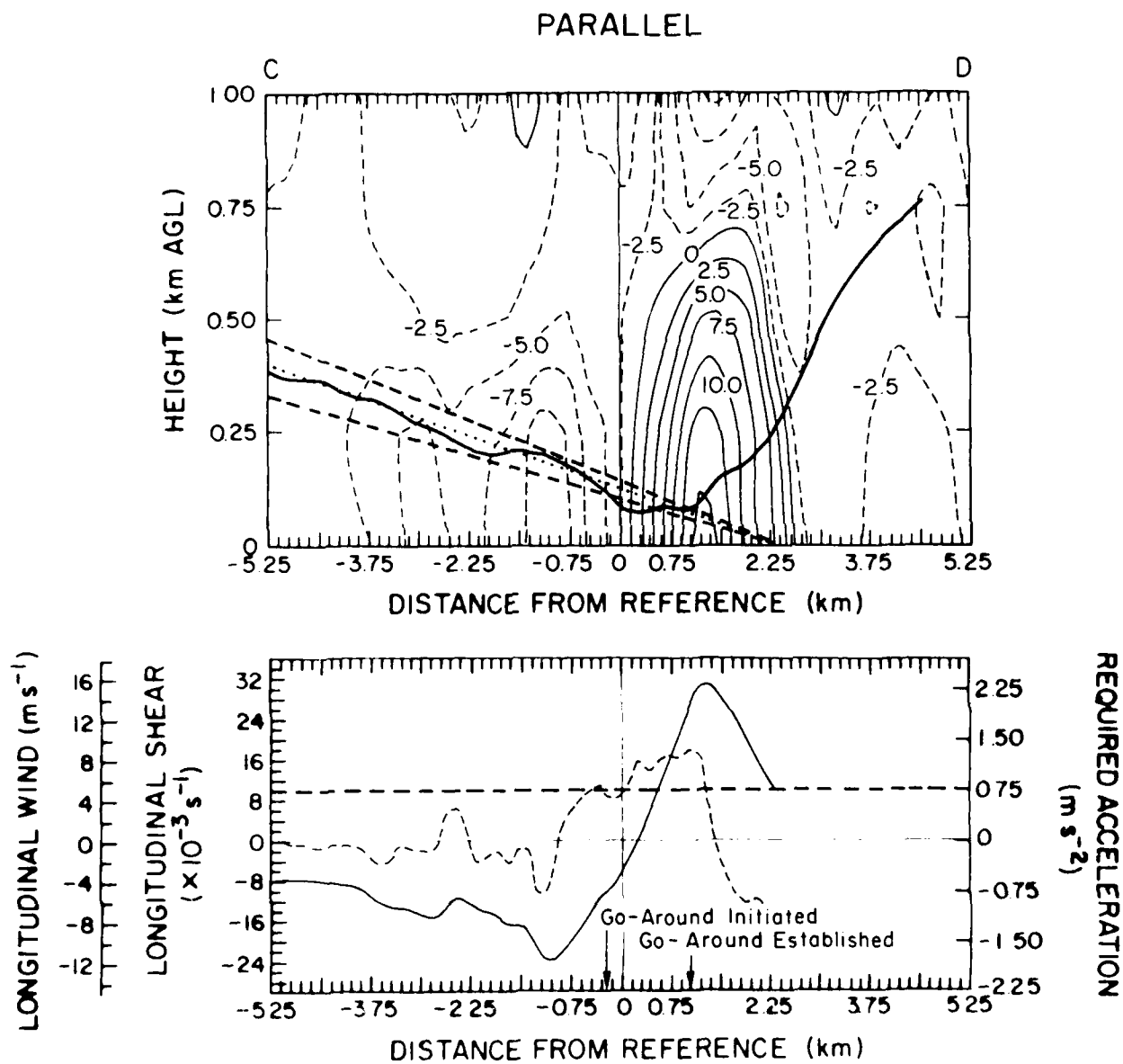
30

FIGURE 10A. Similar to 9a, but for path CD illustrating a Class II case.
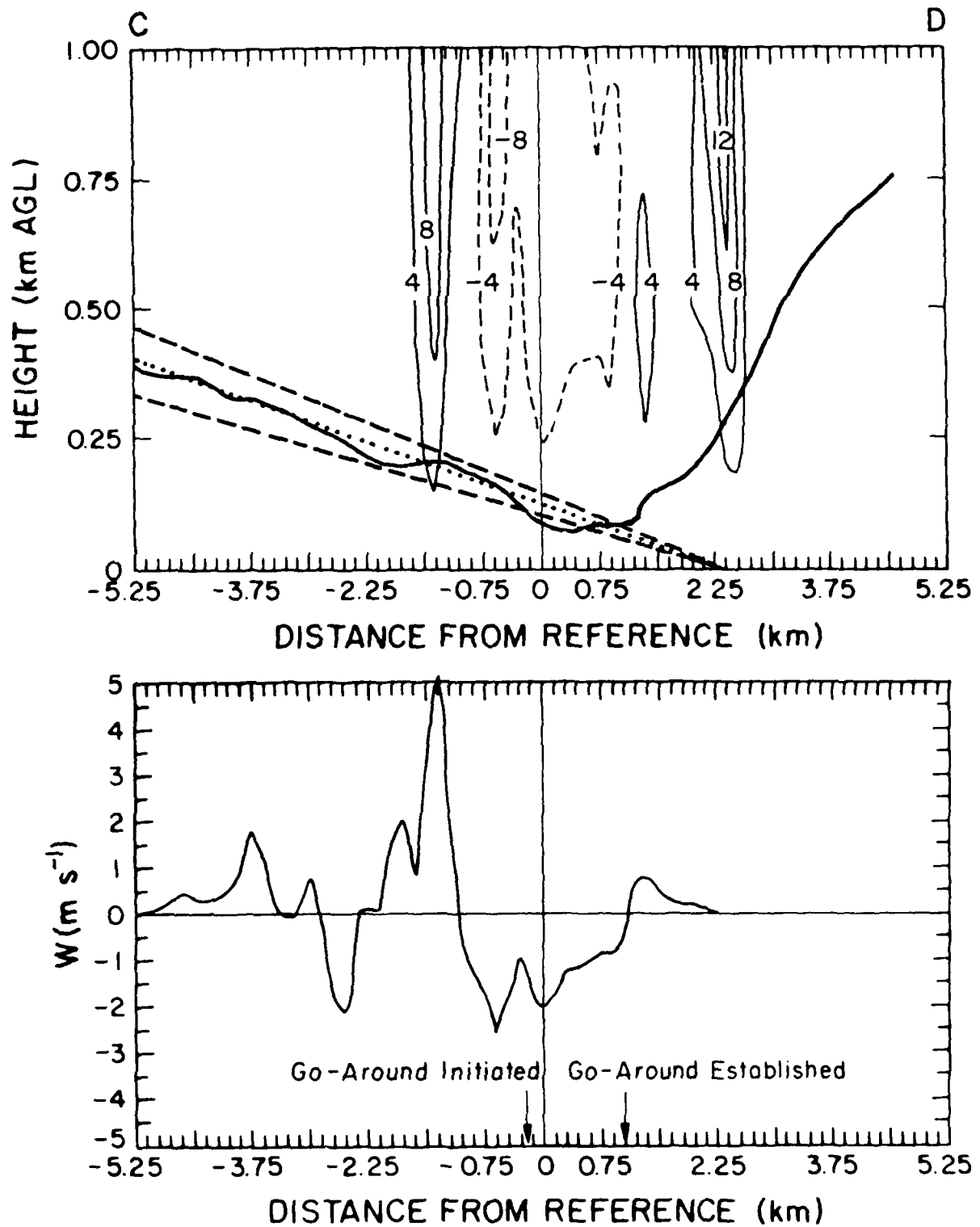
31

VERTICAL VELOCITY

FIGURE 10B. Similar to 9b, but for path CD.

Figures 10a and 10b are similar plots for path CD. This approach takes the model over the reference point at a z_{ref} of 120 m. The model experiences some trouble maintaining this approach path, nearing the go-around threshold at -2.25 km as it passes through a -2 m s^{-1} downdraft. It climbs well above the approach path as it passes through the maximum headwind and strong updraft, on the northwest curl, near -1.2 km. Since the model is above the approach path in a region of relatively strong updraft, engine thrust and pitch are relatively low as it enters the strong shear region. Though the longitudinal shear is not exceeding the performance capability of the model, it is changing faster than the control algorithms can accommodate, *i.e.*, due to the built-in ≈ 2 s delay, the control laws are always behind the required control inputs and cannot catch up. This suggests that gradients of wind shear are important. These factors result in relatively slow but steady descent below the approach path.

At -0.2 km, near an altitude of 100 m, the go-around is initiated. However, the descent is not arrested until the model has descended 75 m further. A climb is established about 0.3 km beyond the reference point, correlating well with the decrease in longitudinal shear below 10×10^{-3} s^{-1} (Figure 10a). This initial climb is of short duration; as longitudinal shear becomes larger, the climb ceases and the model descends slightly, until 1.0 km beyond the reference. There the model experiences the updraft on the southeast curl exiting the positive shear region about 300 m later. At this point, success of the go-around is no longer in doubt, and the model continues without incident.

Examination of the longitudinal shear experienced by the model along paths AB and CD shows that, although the mean longitudinal shear greater than 10×10^{-3} s^{-1} is only slightly larger for path AB than for path CD, a go-around was unsuccessful through AB while it was successful through path CD. This is due to the very rapid change in shear encountered along path AB while the shear slowly increased along path CD. Thus, the control laws could not accomodate the rate at which conditions were changing, degrading system performance.

d. Model Responses to Identical Approach Paths at Different Analysis Times

To investigate model response to different analysis times along path AB, the reference altitude was increased to 200 m. If the 100 m reference altitude were used (as before), the model would impact the ground before the entire response could be experienced. In addition, the go-around algorithm was disabled: no go-around is attempted regardless of how far the model deviates from the desired path. If the go-around algorithm were enabled, escape would be attempted at different places in each analysis, making comparisons between model responses to each analysis time more difficult.

Similar to previous figures, Figs. 11a and 11b show the parallel and vertical components, respectively, for an approach through the 1845 MDT analysis. As the model traverses the strong headwind region, it climbs above the approach path until through the maximum headwind. Near -0.75 km, the model begins to descend below the approach path. Descent is arrested as it passes through the 1.5 m s^{-1} updraft on the northwest curl (Fig. 11b). Immediately after passing into the tailwind side of the microburst—and the region of maximum headwind-to-tailwind shear—the model begins a rapid descent below
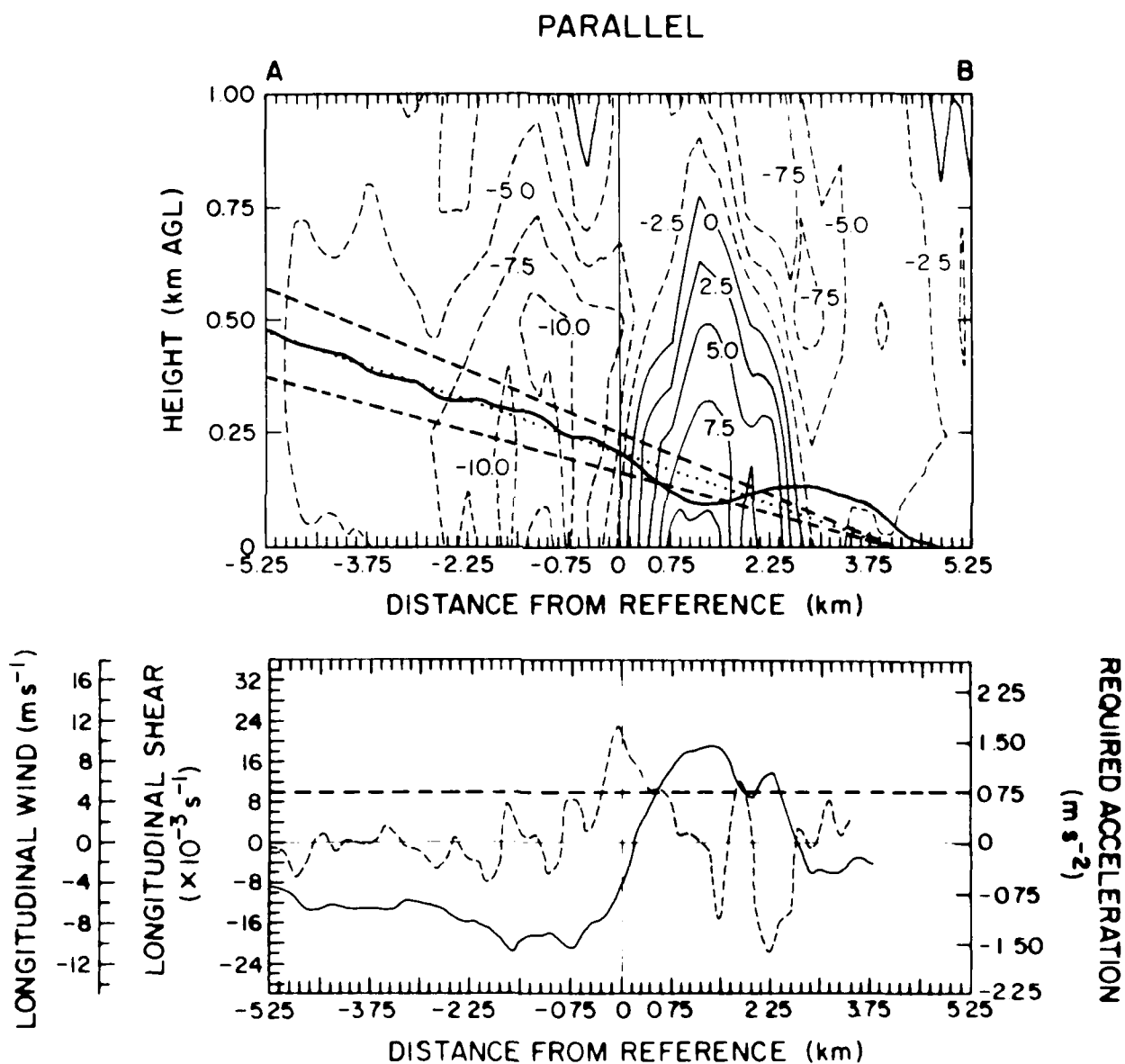
PARALLEL

FIGURE 11A. Modelled flight path along AB plotted on vertical cross section of winds parallel to path for 1845 MDT analysis, similar to previous figures except that z_{ref} = 200 m.
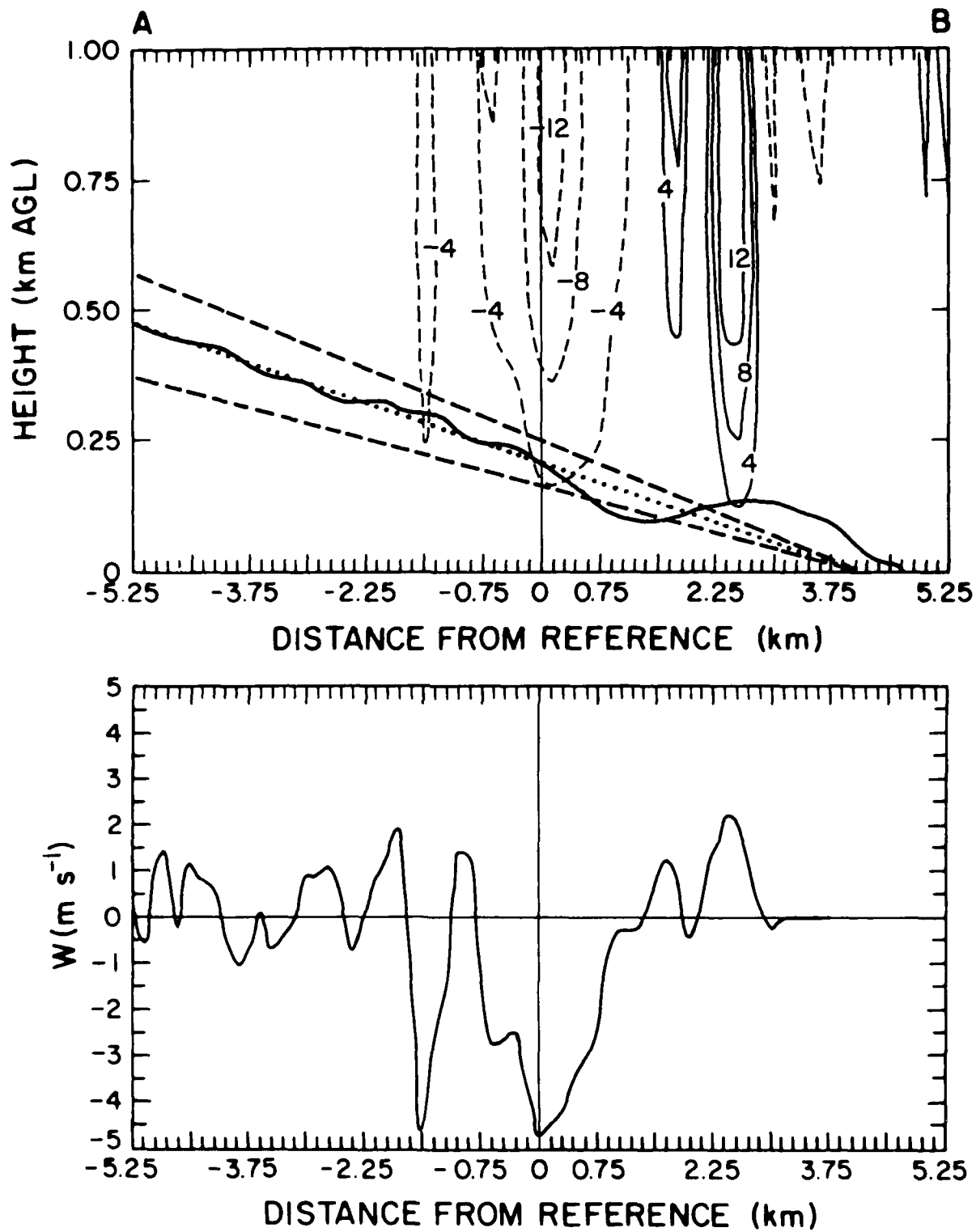
VERTICAL VELOCITY

FIGURE 11B. Modelled flight path along AB plotted on vertical cross section of vertical winds for 1845 MDT analysis, similar to previous figures.

the approach path, enhanced by relatively strong downdrafts (-3 to -4 m s^{-1}). That part of the path over which longitudinal shear exceeds 10×10^{-3} s^{-1} is relatively short with a sharp peak of 23×10^{-3} s^{-1} near the reference point, 0 km. The average value of 14×10^{-3} s^{-1} is 20% less than the average shear over 1.8 km observed at the surface. Near 1.1 km, the descent is arrested as the model exits the region of increasing tailwind, and begins climbing towards the approach path. An increasing headwind and moderately strong updraft on the southeast curl results in substantially increased climb performance. Upon exiting the microburst the model continues climbing well above the approach path as it flies into a rapidly increasing headwind and a relatively strong updraft (2.5 m s^{-1}).

Figures 12a and 12b show the same approach path through the 1847 MDT analysis. Through the headwind maximum, the model tracks the approach path well. Effects of the weaker updraft associated with the northwest curl are still apparent at -1.5 km, where the model rises slightly above the intended trajectory and then descends below it once again. While passing from the headwind to the tailwind side of the microburst, and into a relatively extensive area of downdraft, the model begins to descend below the approach path. Longitudinal shear is somewhat weaker over a shorter distance than in the previous analysis with a 24×10^{-3} s^{-1} peak value near 0.2 km. Because the model is flying through moderate downdrafts prior to encountering strong longitudinal shear, the control laws have partially optimized the modelled entry configuration by means of a high thrust setting as well as a higher-than-nominal pitch angle. Because the control laws have not adjusted the model for updraft and increasing headwind, the altitude loss is not as severe as in the previous example, and the model never strays more than 0.7° below the descent path. Though not intended, this helps illustrate how sensitive the outcome of a microburst penetration is to the modelled entry configuration.

Figures 13a and 13b show the model response of flight through the 1850 analysis. Descent below the approach path occurs as the model passes over -2.25 km due to a large headwind decrease, apparent in the wind and shear plots at the bottom of Fig. 13a, and a strong downdraft (-3.8 m s^{-1}) seen clearly at the bottom of Fig. 13b. The model remains below the approach path, descending further away from it near -0.75 km, reaching the go-around threshold near 0 km. At 0.6 km the model exits the region of longitudinal shear greater than 10×10^{-3} s^{-1} and begins a relatively slow (due to the downdraft) climb back to the approach path. This is another example of a case where the aircraft entered the strong shear region in a high thrust, high pitch condition. The relatively long residence time in the downdraft coupled with moderate average shear values through which the model flew (10×10^{-3} s^{-1} over 1.8 km) created a more serious response than previous paths through stronger wind shear. The long residence time in strong downdraft is expected for this path as seen from Fig. 5b.

During an approach through the 1852 data (Figs. 14a and 14b) the model remains above the approach path, due to strong updrafts between -3.0 km and -1.5 km, until -0.4 km from the reference point. Around -0.75 km it begins experiencing moderate shear, with a 13×10^{-3} s^{-1} peak on the northwest side of the microburst. Recall that by this time the microburst displayed two velocity maxima on either side with relatively calm winds around the center. Two regions of relatively strong longitudinal shear are expected:

FIGURE 12A. Modelled flight path along AB plotted on vertical cross section of winds parallel to path for 1847 MDT analysis, similar to previous figures.

37

VERTICAL VELOCITY

FIGURE 12B. Modelled flight path along AB plotted on vertical cross section of vertical winds for 1847 MDT analysis, similar to previous figures.

FIGURE 13A. Modelled flight path along AB plotted on vertical cross section of winds parallel to path for 1850 MDT analysis, similar to previous figures.

VERTICAL VELOCITY

FIGURE 13B. Modelled flight path along AB plotted on vertical cross section of vertical winds for 1850 MDT analysis, similar to previous figures.
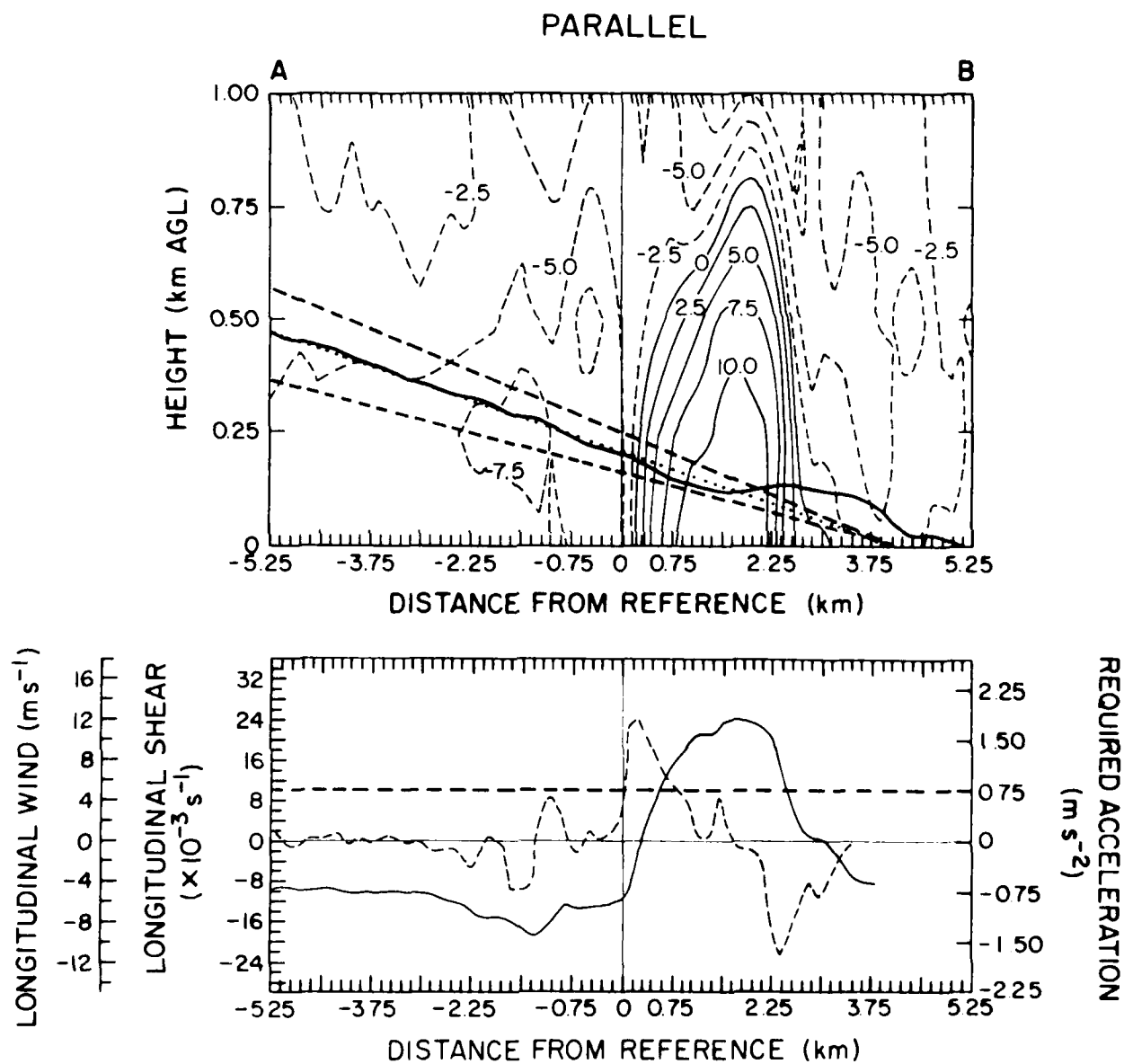
PARALLEL

FIGURE 14A. Modelled flight path along AB plotted on vertical cross section of winds parallel to path for 1852 MDT analysis, similar to previous figures.
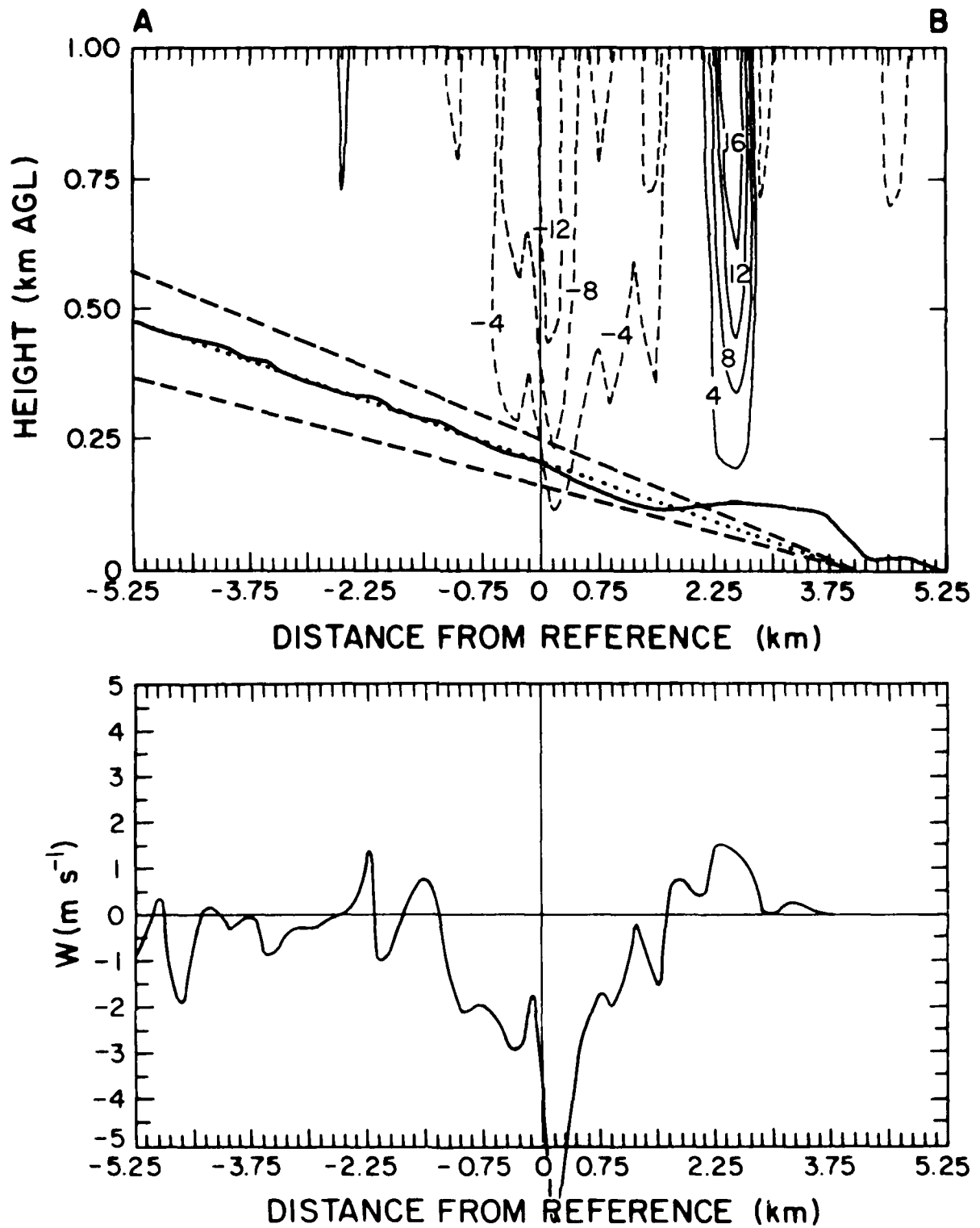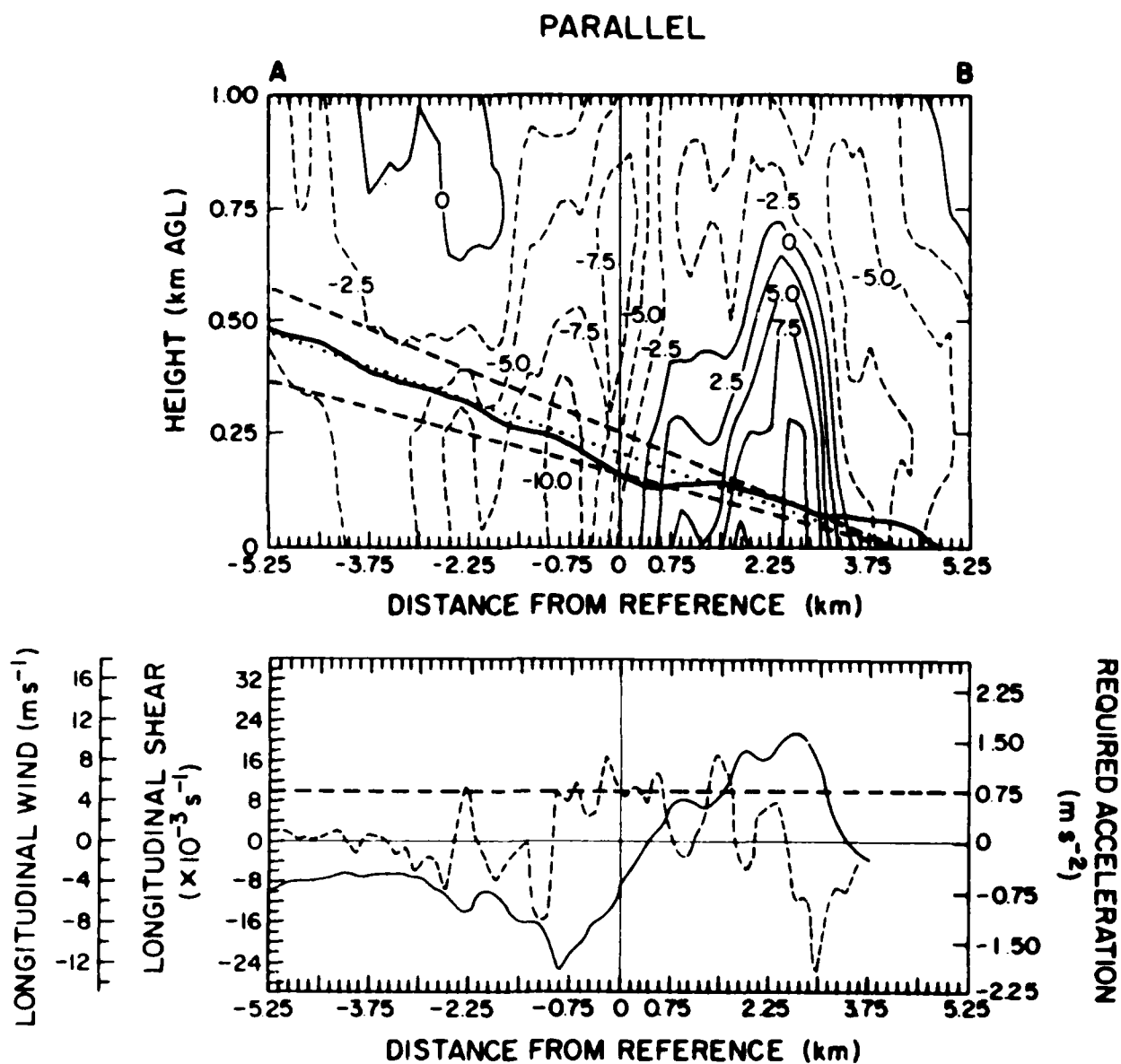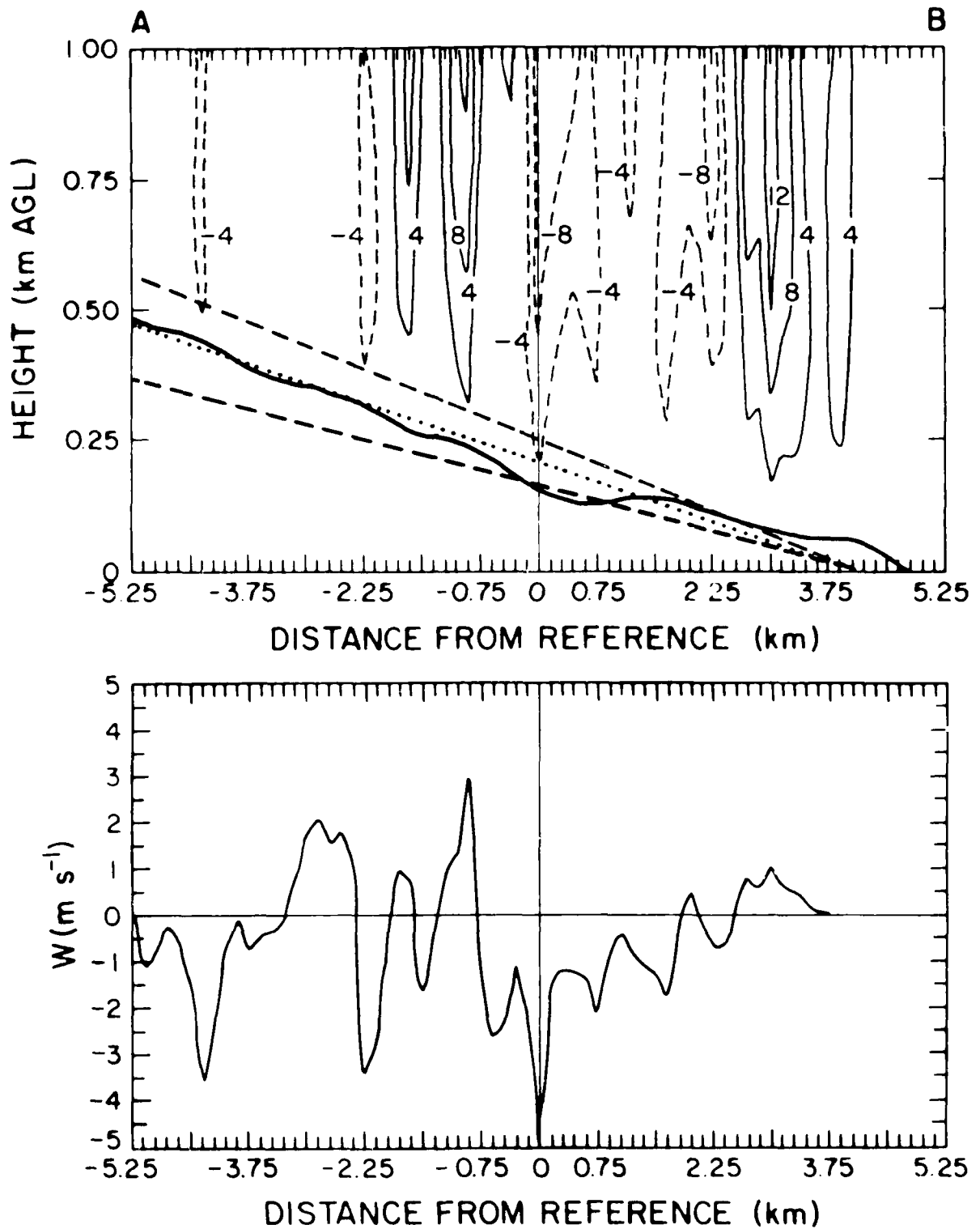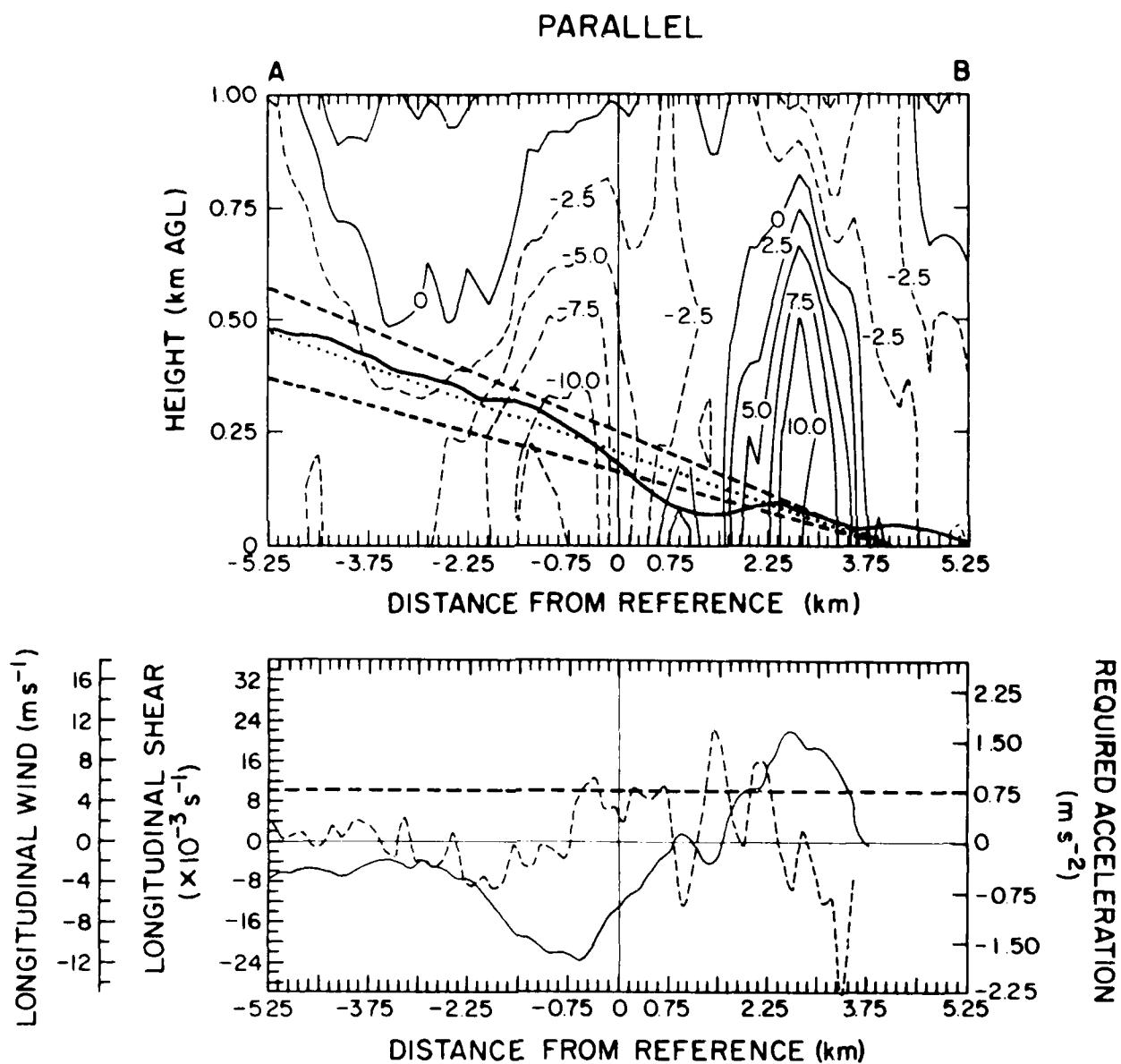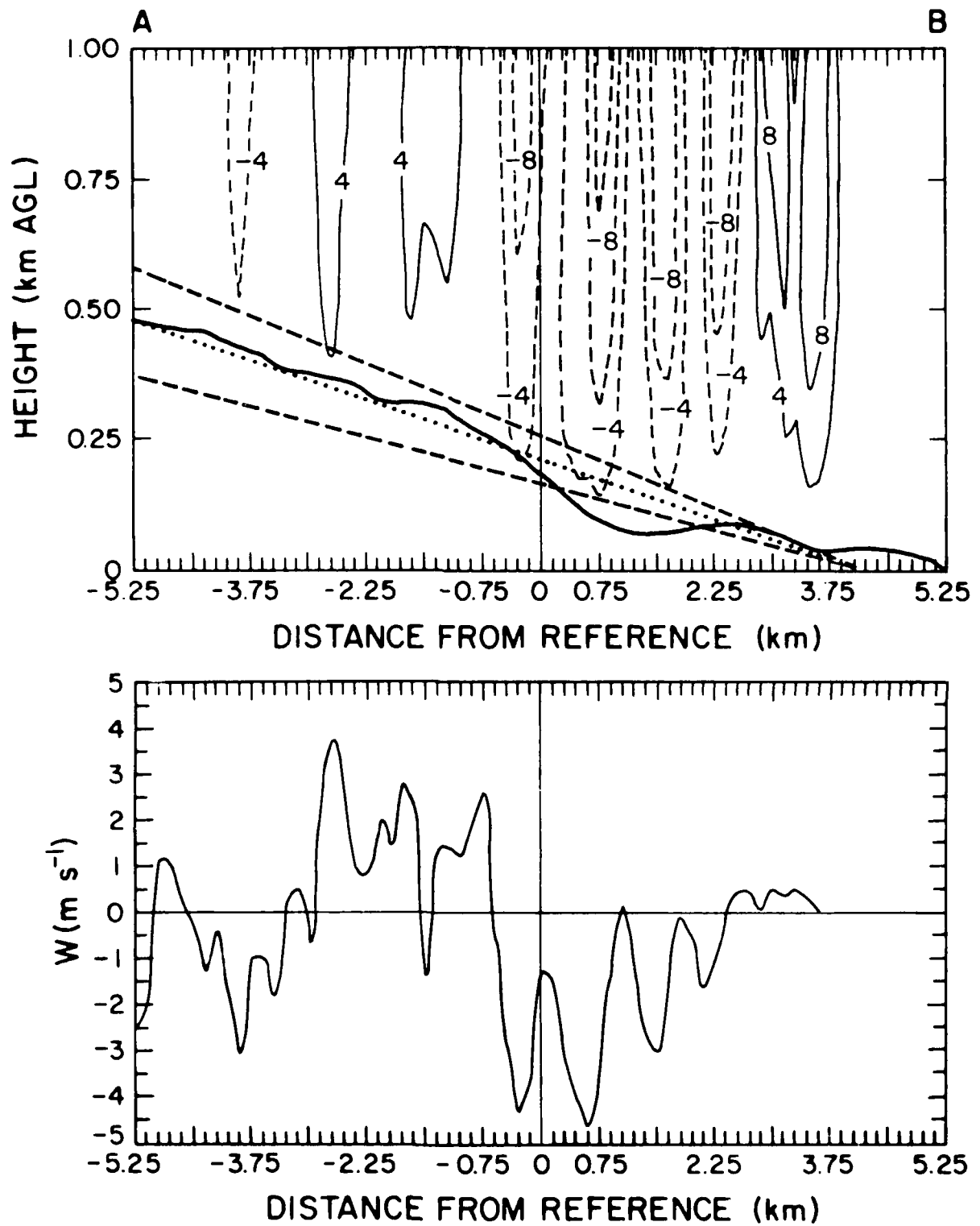
41

VERTICAL VELOCITY

FIGURE 14B. Modelled flight path along AB plotted on vertical cross section of vertical winds for 1852 MDT analysis, similar to previous figures.

42

the first (−2.3 to −0.6 km) associated with a negative peak followed by a positive peak and the second (2.3 to 3.2 km) associated with a positive peak followed by a negative peak. Such a signature appears in the longitudinal shear plotted in Fig. 14a.

The first region is primarily responsible for descent of the model below the approach glide path. Effects of the first shear region are exaggerated by extensive moderate-to-strong downdrafts experienced by the model.

Since apparently minor changes in the analyzed winds produced noticeable differences in the modelled flight path, investigation of time-dependent (Lagrangian) wind fields seemed in order. However, an approach requires about 3 (simulated) min to complete, nearly the temporal data spacing. Further, the region posing the most threat to jet transport aircraft covers only a small portion of the overall flight path. At a nominal approach speed of 70 – 75 m s^{-1} this region is traversed in about 30 s. Changes in the wind field during that time cannot be resolved by these analyses. Subtle differences appeared between Lagrangian simulations centered on an analysis time and an Eularian simulation at the same analysis time, but the differences are not significant.

e. Takeoff Path Examples

In the takeoff control algorithm, the thrust control law increases engine thrust to the rated takeoff value as the model accelerates to an airspeed of 30 m s^{-1}. Thrust is then held constant as the model reaches takeoff speed, when pitch is increased at 3° s^{-1} to a pitch angle of 10°. In calm (nominal) wind conditions the model makes a run of approximately 1.7 km before lifting off and climbing at a 6.4° angle, roughly similar to Boeing 727 aircraft in service.

Location of the reference point is selected relative to this nominal liftoff point and is similar to the approach cases. Figure 15 shows the coordinate convention used for departure cases, similar to Fig. 8. This convention defines z_{ref} as the altitude at which the model will pass over the reference point (x_{ref}, y_{ref}), climbing out along a 6.4° path after a 1.7 km takeoff roll. A negative z_{ref} is possible (since a downward projection of a 6.4° departure path intersects the ground at the nominal liftoff point), indicating the model passes over x_{ref} and y_{ref} before having travelled 1.7 km down the runway.

For every flight path investigated, the model was able to take off without impacting the ground. However, there were many situations where liftoff was only barely achieved and the takeoff would not have succeeded if the computer simulation accounted for obstacles similar to those typically found around an airport.

Figure 16 shows a takeoff simulation along path AB (1847 analysis). A plot of vertical velocity is not included for departure cases since the model remains so close to the ground throughout the critical part of its flight that vertical velocity is less than 1 m s^{-1}. The longitudinal wind and shear plots show values for the actual flight paths taken by the model, since they are well away from the nominal flight path. For this case, the model would nominally pass over the reference point at $z_{ref} = 13$ m (113 m off the departure end of the runway). For figures depicting takeoff simulations, a large, heavy arrow 1.7 km left of the beginning of the nominal departure path marks the takeoff roll origin, i.e.,
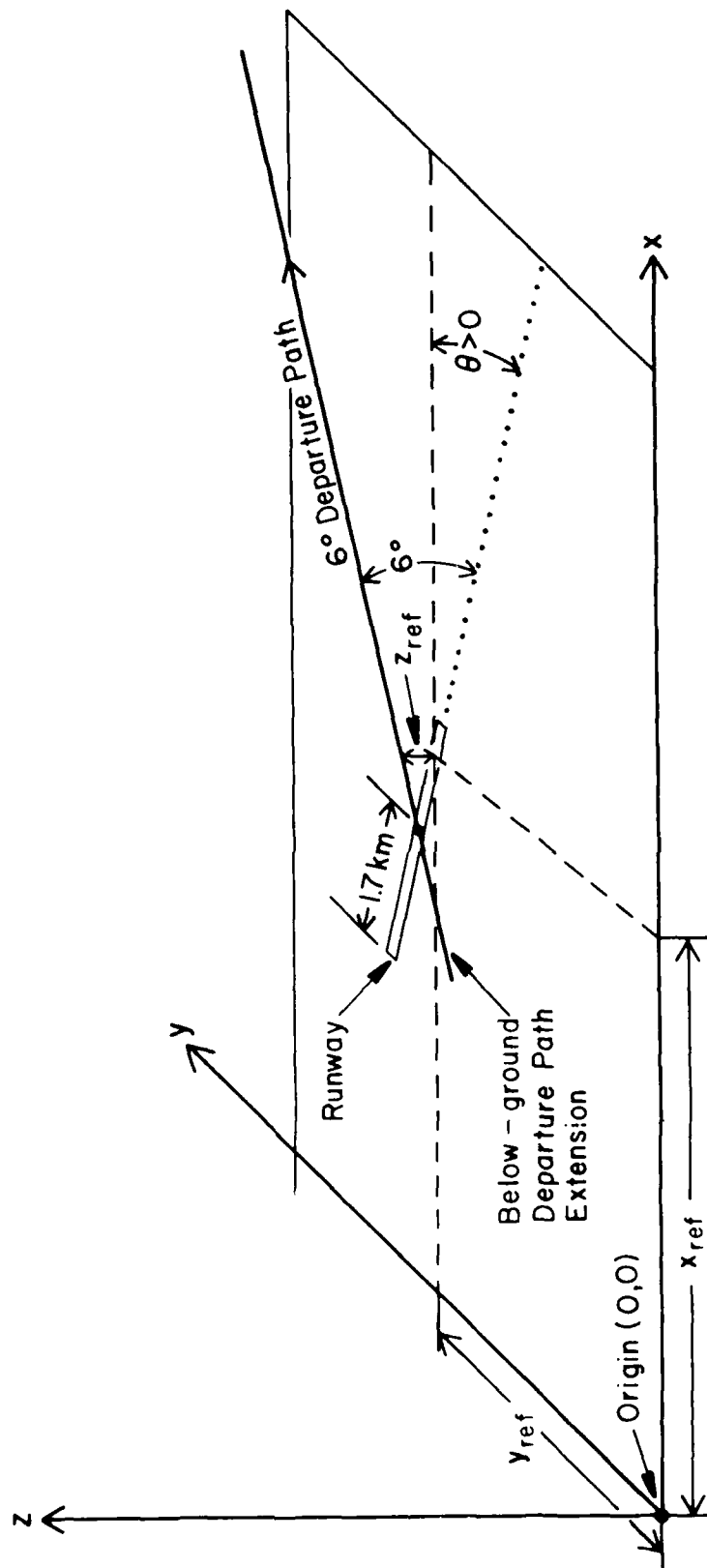
43

FIGURE 15. Coordinate system used to define departure path. The model passes over (x_{ref}, y_{ref}) at height z_{ref} after a nominal departure consisting of a 1.7 km take-off run followed by a $6°$ climbout angle.
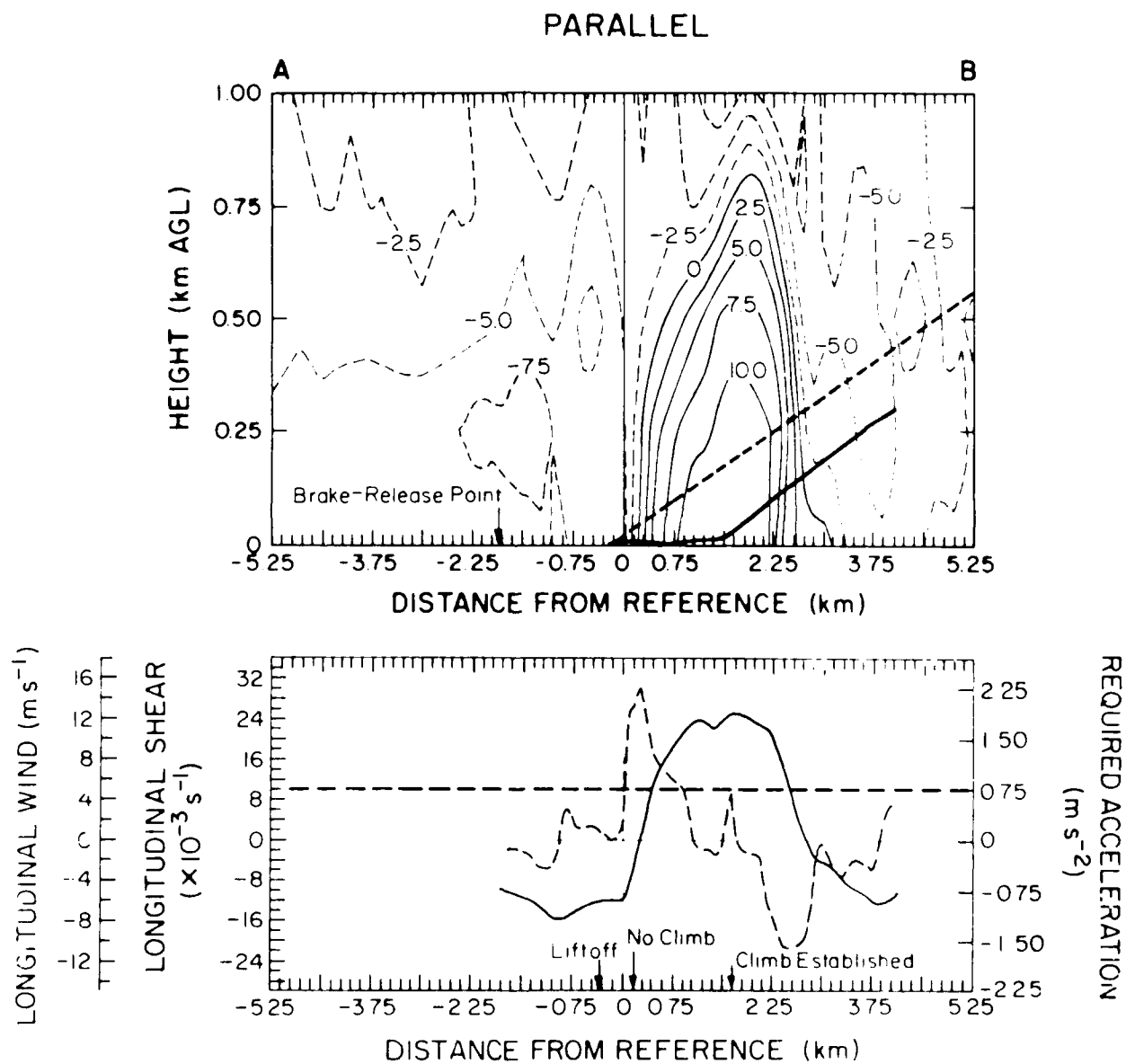
44

PARALLEL

FIGURE 16. Modelled departure for path AB using data from the 1847 MDT analysis illustrating a
Class I case, similar to 9a.

the "brake-release point." During the first 750 m of takeoff roll, the model experiences a performance-increasing shear with a peak of -6×10^{-3} s^{-1}. In the last half of its takeoff roll, it experiences performance-decreasing shear of the same magnitude. Due to the general headwind experienced by the model, it lifts off after a roll of 1.5 km.

Shortly after liftoff, having climbed to about 16 m, it enters a region of strong shear (peak value of 28×10^{-3} s^{-1}) resulting in a complete inability to climb and an altitude loss. Thus the model descends to an altitude of 10 m. Although the model is inertially accelerating, airspeed loss occurs because the headwind is shearing into a tailwind faster than the model can inertially accelerate. A 10 m altitude is barely maintained until about 1 km beyond the reference point, well after where the longitudinal shear becomes weakly positive. A constant climb rate does not occur until 2 km from the point of initial liftoff, because this distance is required for the model to accelerate back to its target airspeed. This is a Class I (most difficult) departure case and and is similar to the PAA Flight 759 accident (Fujita, 1983a), lacking only an obstruction off the departure end of the runway.

Figure 17 shows a takeoff simulation along path IJ of the 1847 analysis, judged representative of a Class II (moderately difficult) departure case. For path IJ, z_{ref} is -31 m corresponding to a horizontal position 283 m before the nominal liftoff point. The model starts its takeoff roll in a weak headwind (-3 m s^{-1}) with little shear. After travelling 1.2 km down the runway, longitudinal shear sharply increases, resulting in a slightly longer-than-nominal takeoff roll (1.8 km). The model then climbs at an angle shallower than $6.4°$ because it is climbing in performance-decreasing shear. The longitudinal shear component remains stronger than 10×10^{-3} s^{-1} for about 500 m, when it rapidly changes sign and aids the modelled climb performance.

Microburst location relative to the liftoff point was felt to be critical to modelled takeoff performance. Figure 18 clearly illustrates the effect of microburst location during takeoff. Three curves are plotted for path CD (1847 analysis) where the microburst is encountered at $z_{ref} = -6$ m (path A), $z_{ref} - 32$ m (path B), and z_{ref} 64 m (path C) altitudes.

When the microburst is encountered early in the takeoff roll (z_{ref} 6 m, 57 m before the nominal liftoff point), the model requires a long takeoff roll prior to liftoff, slightly over 2.0 km, and does not lift off until most of the maximum shear region is traversed. After takeoff, it climbs at a slow but steady rate as it passes through the strongest shear ($17 \cdot 10^{-3}$ s^{-1}). When through the maximum tailwind point (1.2 km beyond the reference point) where the shear changes sign and becomes performance-increasing, the climb angle increases and the model resumes a normal departure profile.

If the reference point intersects the calm-condition departure path at $z_{ref} - 32$ m (287 m beyond the calm-condition liftoff point), a somewhat different scenario develops. The model experiences an increasing headwind for the first 750 m of its takeoff roll, afterwards entering a strong ($\cdot 10 \cdot 10^{-3}$ s^{-1}) shear region. The model lifts off 150 m beyond the reference point as it enters the region of strongest shear (average value $16 \cdot 10^{-3}$ s^{-1}). Although the model is losing airspeed during this time, the loss is not severe enough to immediately arrest its climb. Airspeed is slowly lost until the model has insufficient lift

PARALLEL
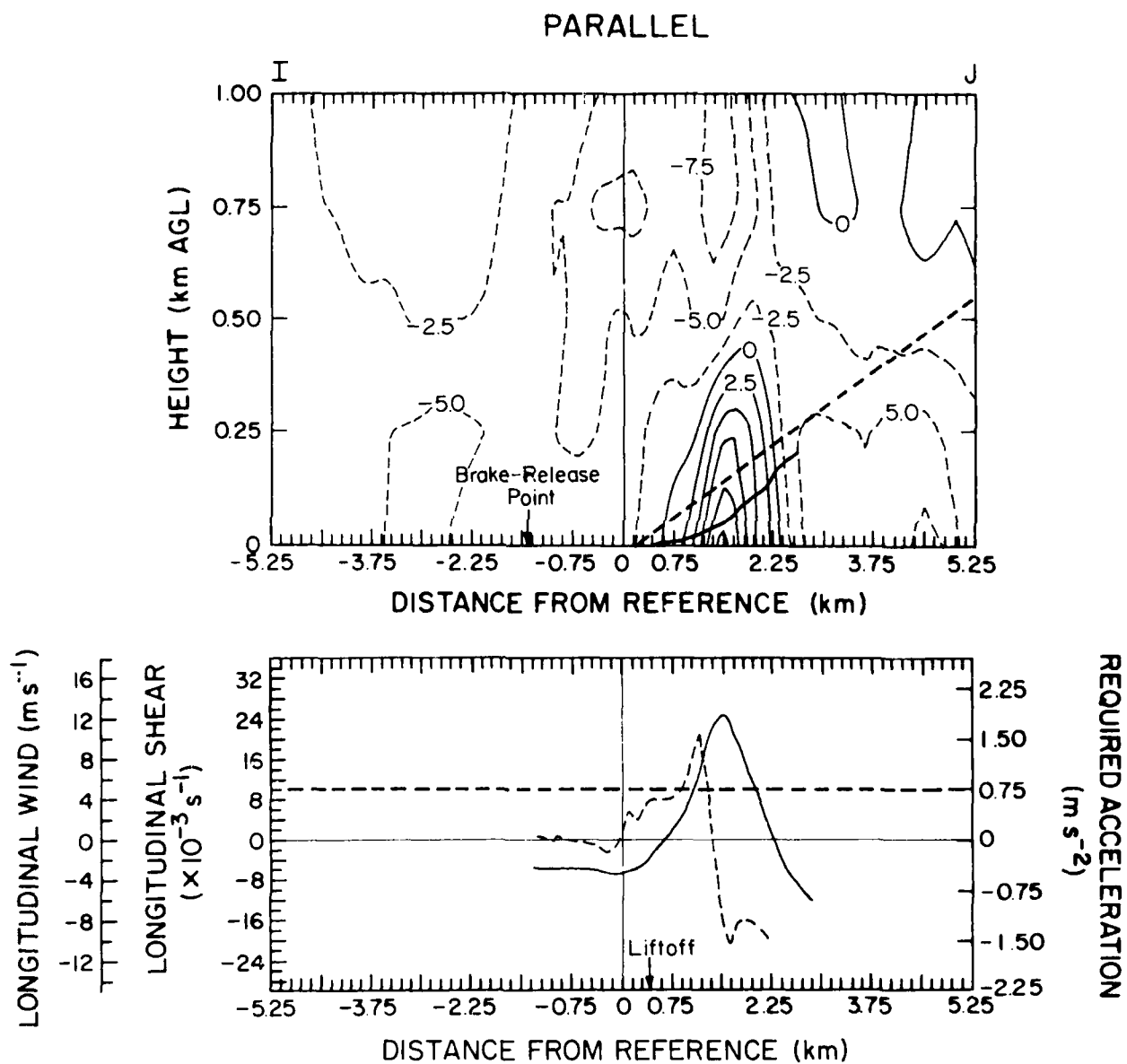
FIGURE 17. Modelled departure for path IJ using data from the 1847 MDT analysis illustrating a Class II case.

47

PARALLEL

C   D

HEIGHT (km AGL)

Brake-Release
Points
C B A

DISTANCE FROM REFERENCE (km)

PATH A

LONGITUDINAL WIND (m s⁻¹)
LONGITUDINAL SHEAR (×10⁻³ s⁻¹)
REQUIRED ACCELERATION (m s⁻²)

Liftoff

PATH B

Liftoff No Climb
Climb Reestablished

PATH C

Climb
Reestablished
Liftoff No Climb

DISTANCE FROM REFERENCE (km)

FIGURE 18. Modelled departure along path CD showing effect of different microburst locations relative to runway on modelled performance.

48

(due to insufficient airspeed) to continue climbing. A small altitude loss, assisted by weak downdraft (-0.6 m s^{-1}), occurs as flight through the shear region continues. Upon exiting the shear region a climb is not immediately reestablished, even though the model is in an area of strong negative shear (average value -13×10^{-3} s^{-1}). Some time is required for the model to accelerate to its target airspeed.

In the final case, where the microburst center is encountered at 64 m nominal departure altitude (567 m beyond the nominal liftoff point), a flight path similar to the previous case is obtained. Because the shear region is encountered later than i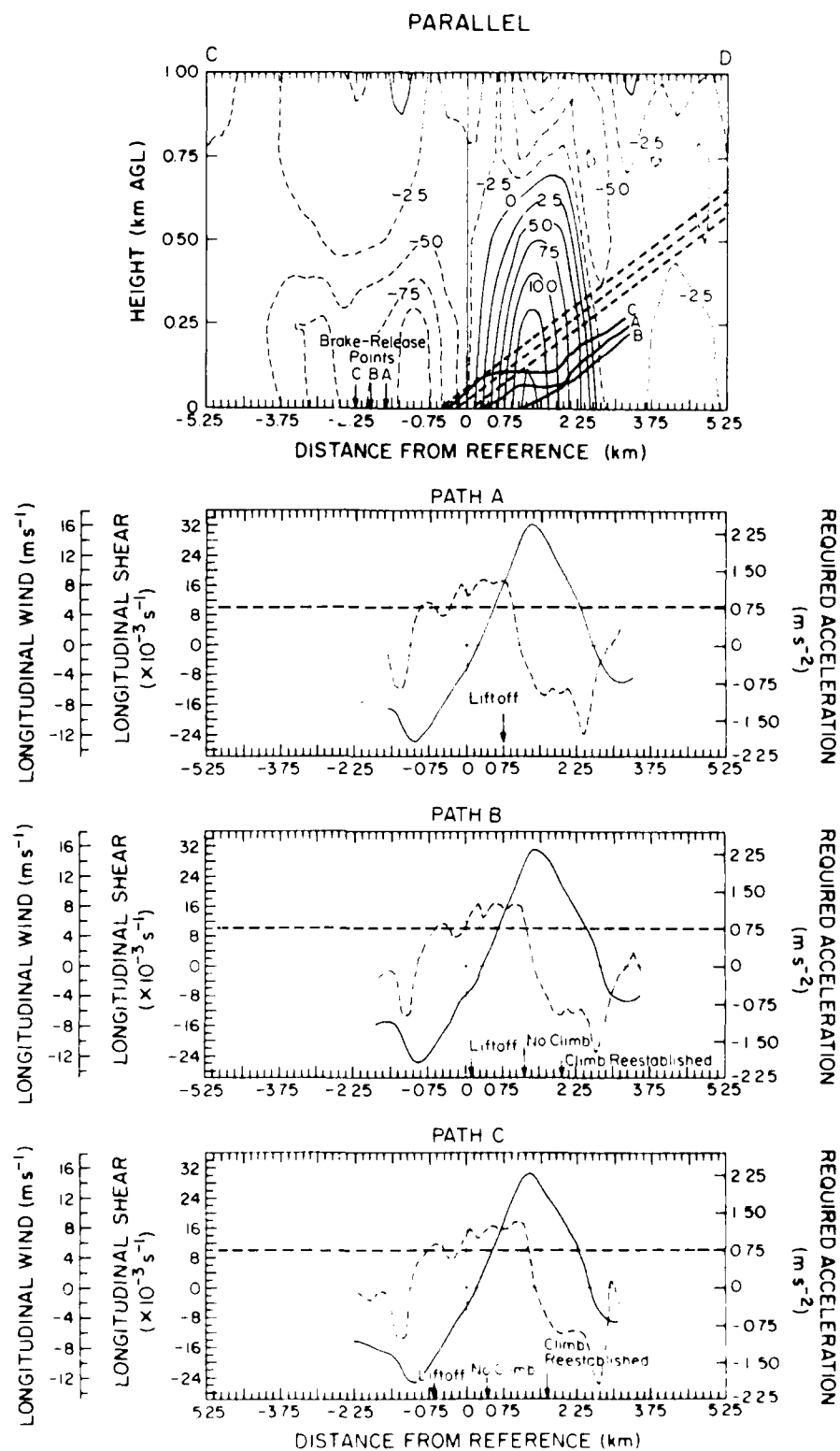n previous cases, the model climbs to a higher altitude before entering the area of strong shear and relatively strong (-1.4 m s^{-1}) downdraft. Since the area of appreciable downdraft covers a larger area aloft than near the ground, the model suffers an earlier loss of climb ability than in case B. Classification of this path is obviously dependent upon where the microburst is located with respect to the runway; these cases range from Class I (most difficult) to Class II (moderately difficult) encounters.

f. Gust Fronts

A significant response is noted as the model exits a region of tailwind (the microburst boundary) in nearly all cases. An excellent example is provided by the approach case shown in Figures 12a and 12b (path AB, $z_{ref} = 200$ m, 1847 analysis, go-around algorithm disabled). At 2.25 km the model rapidly climbs above the intended flight path as it experiences a moderate updraft and rapidly increasing headwind. This is equivalent to the response an aircraft experiences as it traverses a gust front.

Gust fronts are an inherently performance-increasing wind shear; an aircraft invariably experiences a headwind increase and an updraft as a gust front is traversed, regardless of the direction from which the gust front is approached. However, gust front boundaries are often quite turbulent. Furthermore, after the aircraft has stabilized in the new environmental winds, the resulting descent profile relative to the ground will be steeper than the descent profile prior to gust front entry unless the aircraft configuration is altered. The turbulence and steepened descent profile can result in impact short of the runway.

4. Summary and Conclusions

Serial multiple Doppler analyses of a microburst were gathered during JAWS and analyzed yielding three-dimensional winds of unprecedented spatial and temporal resolution at heights to 1 km within a microburst. These data were then used as input to a diagnostic numerical aircraft model that grossly resembles Boeing 727-type aircraft. Simulated flight through the microburst yielded realistic results, as judged from previous jet transport wind shear accidents. Realism of this data is derived both from its intrinsic three-dimensionality and from the nature of the wind field recovery, which was performed with a minimum of limiting assumptions. In one case, results mimicked a documented departure accident (PAA Flight 759), while an approach had similarities to a documented approach accident (EAL Flight 66). Qualitatively, microburst winds resulting from a multiple Doppler radar synthesis affect numerically modelled jet transport aircraft flight in a

similar manner to actual microburst winds and jet transport aircraft. This reinforces the credibility of three-dimensional winds derived from multiple Doppler analysis.

Microburst penetration altitude during approach or departure is a critical factor. If encountered at sufficiently low altitude, a go-around may be impossible due to the high descent rates induced. Depending upon the encounter height during takeoff, the takeoff roll may require an excessive amount of runway, or an aircraft may not be able to climb at a steep-enough angle after liftoff to clear obstacles around the airport.

This has serious implications for any kind of ground-based detection and warning system, because aircraft performance is sensitive to where along the approach or departure path wind shear is encountered. Any warning to pilots must include relatively precise location information. It is not practical to close or restrict traffic flow at a major airport because there is a wind shear located "somewhere" on the airport. Aircraft fly very well defined paths in the immediate airport vicinity, so only wind shear threats near those paths need serious attention. This also avoids "false alarms," thus rendering warnings effective.

The downdraft associated with a microburst need not be overwhelming to cause an accident. The threat to jet transport aircraft lies in the association of only moderate (≈ 4 m s^{-1}) downdrafts combined with horizontal wind shear, especially when the approximate in-flight acceleration capability is exceeded by the product of desired penetration airspeed and horizontal shear magnitude. Downdraft intensity generally decreases as the ground is approached, becoming zero at the ground. Relatively strong downdrafts may exist near the ground in some cases.

Mean shear over a path is not as important to modelled results as peak shear values along the path. For this model and its control laws, a rapidly increasing, strong ($> 20 \times 10^{-3}$ s^{-1}) longitudinal shear followed by weaker, but significant ($> 10 \times 10^{-3}$ s^{-1} but $< 20 \times 10^{-3}$ s^{-1}) shear is more difficult to traverse than shears that increase slowly to significant values. This is partially an artifact of response time as specified in the control laws. This is also a function of aircraft configuration as it enters the significant shear region. If entered in a high-thrust, high-pitch configuration, the flight path will suffer smaller deviations below the desired approach path. Emphasis is placed on the fact that the control laws used in this study utilize no energy trade techniques and do not think ahead, i.e., trade kinetic energy for altitude or change their basic strategy when certain clues occur, such as a rapid, unexplained increase in airspeed and/or climb rate.

Longitudinal wind differential or mean longitudinal wind shear along the nominal approach path proved to be a good approximation of the winds that the model encountered. This is because the model never deviated significantly from the nominal approach path (except in the case of a successful go-around). The same is not true of departure cases since the model deviates significantly from the nominal path, due to an inability to climb at a steep-enough angle. A secondary factor is increased distance often required for takeoff rolls.

50

The results obtained with multiple Doppler derived wind fields are likely to be much more realistic than results obtained using wind fields derived from tall instrumented towers or flight data recorders. The JAWS effort represents the first time multiple Doppler analyses have been applied to any kind of flight simulation.

These data are available to the community at-large on magnetic tape through NCAR for use in simulator training, aircraft performance, control theory research, and detection and warning equipment and algorithm development.

Acknowledgments

51

References

Byers, H. R., and R. R. Braham, 1949: The thunderstorm. U.S. Government Printing Office, 287 pp.

Caracena, F., R. A. Maddox, J.F.W. Purdom, J. F. Weaver, R. N. Green, 1983: Multi-scale analyses of meteorological conditions affecting Pan American World Airways Flight 759. NOAA Tech. Memo. ERL ESG-2, Environmental Sciences Group, Boulder, Colo., 45 pp.

Department of Transport, Australia, 1977: Accident investigation report-Fokker Friendship F-27-100 Aircraft VH-EWL at Bathurst, New South Wales, on 31 May 1974. Special Investigation Report No. 76-2. Department of Transport, Air Safety Investigation Branch, Canberra, New South Wales, Australia. October, 1976, 24 pp.

Doviak, R. J., P. S. Ray, R. G. Strauch, L. J. Miller, 1978: Error estimation in wind fields derived from dual Doppler radar measurements. *J. Appl. Meteor.*, **15**, 868-878.

Foy, W. H., 1979: Airborne aids for coping with low-level wind shear. FAA Report No. FAA-RD-79-117, U.S. Dept. of Transportation, FAA, Washington, D.C., 96 pp.

Frost, W., H. P. Chang, J. McCarthy, K. L. Elmore, 1985: Aircraft performance in a JAWS microburst. *J. Aircraft*, **22**, 561-567.

Frost, W., and R. L. Bowles, 1984: Wind shear terms in the equations of aircraft motion. *J. Aircraft*, **21**, 866-872.

Frost, W., and D. W. Camp, 1977: Wind shear modelling for aircraft hazard definition. FAA Interim Report FAA-RD-77-36, Systems Research and Development Service, Washington, D.C., 139 pp.

Frost, W., 1983: Flight in low-level wind shear. NASA Contractor Report 3678, 107 pp.

Fujita, T. T., 1976: Spearhead echo and downburst near the approach end of a John F. Kennedy Airport runway, New York City. University of Chicago, Department of Geophysical Sciences, Satellite and Mesometeorology Research Project. SMRP Research Paper 137, University of Chicago, 51 pp.

Fujita, T. T., 1983a: Microburst wind shear at New Orleans International Airport, Kenner, Louisiana, on July 9, 1982. University of Chicago, Department of Geophysical Sciences, Satellite and Mesometeorology Research Project. SMRP Research Paper 199, University of Chicago, 39 pp.

Fujita, T. T., 1983b: Andrews AFB microburst. University of Chicago, Department of Geophysical Sciences, Satellite and Mesometeorology Research Project. SMRP Research Paper 205, University of Chicago, 36 pp.

Fujita, T. T., and F. Caracena, 1977: An analysis of three weather-related aircraft accidents. *Bull. Am. Meteor. Soc.*, **58**, 1164-1181.

Fujita, T. T., and H. R. Byers, 1977: Spearhead echo and downburst in the crash of an airliner. *Mon. Wea. Rev.*, **105**, 129-146.

Goff, R. C., 1975: Thunderstorm-outflow kinematics and dynamics. NOAA Tech. Memo ERL NSSL-75, National Severe Storms Laboratory, Norman, Okla., 63 pp.

Kessinger, C., M. Hjelmfelt, J. Wilson, 1983: Low-level microburst wind structure using Doppler radar and PAM data. Preprints, 21st Conf. on Radar Meteorology, Am. Meteor. Soc., Boston, Mass., 609-615.

Leise, J. A., 1981: A multidimensional scale-telescoped filter and data extrapolation package. NOAA Tech. Memo. ERL WPL-82, Wave Propagation Laboratory, Boulder, Colo., 20 pp.

McCarthy, J., E. F. Blick, R. R. Bensch, 1979: Jet transport performance in thunderstorm wind shear conditions. NASA Contractor Report 3207, NASA, Washington, D.C., 61 pp.

McCarthy, J., J. Wilson, T. T. Fujita, 1982: The Joint Airport Weather Studies Project. *Bull. Am. Meteor. Soc.*, **63**, 15-22.

National Research Council, 1983: Low-altitude wind shear and its hazard to aviation. National Academy Press, Washington, D.C., 161 pp.

National Transportation Safety Board, 1976: Aircraft accident report-Eastern Airlines, Inc., Boeing 727-225, N8845E, John F. Kennedy International Airport, Jamaica, New York, June 24, 1975. NTSB Report No. NTSB-AAR-76-8. National Transportation Safety Board, Washington, D.C., March 12, 1976, 47 pp.

National Transportation Safety Board, 1983: Aircraft accident report-Pan American World Airways, Inc., Clipper 759, Boeing 727-235, N4737, New Orleans International Airport, Kenner, Louisiana, July 9, 1982. NTSB Report No. NTSB-AAR-83-2. National Transportation Safety Board, Washington, D.C., March 25, 1983, 115 pp.

Roberts, R. D., and J. W. Wilson, 1984: Precipitation and kinematic structure of microburst producing storms. Preprints, 22nd Conf. on Radar Meteorology, Am. Meteor. Soc., Boston, Mass., 71-76.

Turkel, B. S., P. A. Kessel, W. Frost, 1981: Feasibility study of a procedure to detect and warn of low-level wind shear. NASA Contractor Report 3480, Marshall Space Flight Center, Huntsville, Ala., 70 pp.

Wilson, J. W., R. D. Roberts, C. J. Kessinger, J. McCarthy, 1984: Microburst wind structure and evaluation of Doppler radar for airport wind shear detection. *J. Clim. and Appl. Meteor.*, **23**, 898-915.

END

DATE
FILMED

DEC.

1987